universität wien

DIPLOMARBEIT / DIPLOMA THESIS

Titel der Diplomarbeit / Title of the Diploma Thesis

„The behaviour of the height of the mechanically driven atmospheric boundary layer derived from idealized WRF simulations“

verfasst von / submitted by

Alina Schuster

angestrebter akademischer Grad / in partial fulfilment of the requirements for the degree of

Magistra der Naturwissenschaften (Mag.rer.nat.)

Wien, 2019 / Vienna, 2019

Studienkennzahl lt. Studienblatt / degree programme code as it appears on the student record sheet:	A 190 412 406
Studienrichtung lt. Studienblatt / degree programme as it appears on the student record sheet:	Lehramtsstudium UF Physik UF Mathematik
Betreut von / Supervisor:	Univ.-Prof. Dr. Petra Seibert

Contents

Abstract . . .
Zusammenfassung . . .

1. Introduction **1**
1.1. Atmospheric boundary layer and definitions of atmospheric boundary layer height . 1
1.2. Methods for the determination of the mixing height . . . 3
1.2.1. Overview of methods . . . 3
1.2.2. Remote-sensing-based methods . . . 5
1.2.3. Methods using surface data and parametrisation . . . 6
1.3. The Coriolis parameter in diagnostic equations and parameterisation schemes . . . 9
1.4. Closure schemes and turbulent kinetic energy . . . 13

2. Method for studying ABL height behaviour **17**
2.1. WRF Model . . . 17
2.2. Physics package and parametrisation scheme for this research . . . 21
2.3. Post-processing utilities . . . 26

3. Results **27**
3.1. TKE and potential temperature . . . 27
3.2. Mixing height simulated by the idealised SCM model with zero heat flux . . . 31
3.3. Conclusion . . . 45

A. NCL and Python scripts **46**
A.1. NCL Script: potential temperature vs time and height . . . 46
A.2. Python script: mixing height, friction velocity and other variables . . . 48

List of Tables

1. Some diagnostic equations for the calculation of mixing height. . . . 7
2. Correlation coefficient r between the relevant quantities and the FPC. . . . 12

3. Summary of WRF ABL parameterization schemes . . . 21
4. Surface layer scheme options available in SCM model . . . 23
5. Land surface model options . . . 23
6. Physics options chosen for this work, namelist input file . . . 24
7. Supported post-processing packages . . . 26

8. A sample input sounding file. . . . 32
9. Initial potential temperature profile for cases depicted in Figure 32. . . . 37

List of Figures

1. The structure and the diurnal cycle of the boundary layer. . . . 2
2. The structure of the boundary layer over a rough surface. . . . 2

3. Balance of forces acting on air parcels near the surface and above the friction layer. 3
4. Rotating disc. Coriolis force acting on objects that move along the meridian. 9
5. Definition of geographical latitude and longitude. 10
6. Variation of the Coriolis parameter with latitude. 11
7. Mixing height as a function of latitude as described by Equation 3 11
8. Shear production of turbulence. 15

9. Flowchart for the WRF Modeling System, Version 3 18
10. Idealised cases, more information. 19
11. Potential temperature vs time and height calculated with MYJ and YSU schemes (3 days) 25
12. Potential temperature vs time and height calculated with MYJ and YSU schemes (30 days) 25

13. An example of a TKE-plot calculated with WRF and processed by NCL. 27
14. An example of a potential temperature plot calculated with WRF and processed by NCL. 28
15. Maximum TKE as a function of latitude within 30 days for four seasons. 29
16. Maximum mixing height as a function of latitude within 30 days for four seasons. . 29
17. Maximum TKE as a function of latitude within 30 days for 4 seasons between 30°S und 30°N 30
18. Maximum mixing height as a function of latitude within 30 days for four seasons between 30°S und 30°N 31
19. TKE and potential temperature as a function of time and height. 33
20. The time series of mixing height calculated by model and from Eq. 3 using u_* . . . 34
21. Mixing height as a function of latitude for three wind speeds calculated by model (top) and from Eq. 3 using u_*. 35
22. Mixing height obtained by model and from Eq. 3 using u_* for three wind speeds. Logarithmic scale. 36
23. Ratio of mixing height h_{mix} calculated by model to friction velocity u_* as a function of $1/f$ for three wind speeds. Logarithmic x-axis. 36
24. Mixing height as a function of latitude derived from model simulations and from different diagnostic equations. 37
25. Mixing height as a function of initial wind speed for two latitudes: calculated by model and from Eq. 3 using u_*. 38
26. Mixing height as a function of friction velocity u_* for two latitudes calculated by model and from Eq. 3 using u_*. 39
27. Mixing height (model) versus mixing height (from Eq. 3 using u_*) for three initial wind speeds. 40
28. Mixing height calculated by the model as a function of initial wind speed for three values of the Brunt-Väisälä frequency for two latitudes. 41
29. Mixing height calculated with equation 3 using u_* from model output as a function of initial wind speed for three values of the Brunt-Väisälä frequency for two latitudes 42
30. Mixing height as a function of Brunt Väisälä frequency for three latitudes. Initial wind speed u=10 m/s. 43
31. Mixing height as a function of friction velocity for ϕ=20° and two values of N. 43

32. Mixing height versus initial wind speed calculated by model and via different diagnostic equations. 44

Abstract

Mixing height or atmospheric boundary layer height is an important parameter of the atmospheric boundary layer. There are different possibilities for mixing height determination, the analysis of profile measurements and the application of parameterizations or models. In the present diploma thesis, the problem of estimation of mixing height in situations where mechanically produced turbulence is important was studied. Many simple diagnostic equations for determination of mixing height in such conditions contain the Coriolis parameter. The main question of this study was the performance of such equations in the equatorial areas, where this parameter is zero, and the relevance of the Coriolis parameter for the determination of mixing height. For this purpose, the numerical Weather Research and Forecasting Model (WRF) was employed. Numerical simulations were made with the idealized single-column model version (SCM). It was shown that simple diagnostic equations have a good agreement with the model in higher latitudes, but are unable to estimate mixing height in the equator areas. It was also shown that the Coriolis parameter is less relevant for estimating the stable and near-neutral boundary layer height than initial wind speed, friction velocity, and Brunt-Väisälä frequency.

Kurzfassung

Die Mischungshöhe oder Höhe der atmosphärischen Grenzschicht ist ein grundlegender Parameter der atmosphärischen Grenzschicht. Es gibt verschiedene Methoden, mit denen man die Mischungshöhe bestimmen kann. Man kann sie aus Profilmessungen ableiten, mit Parametrisierungen bestimmen, oder mittels numerischer Modelle erhalten. In der vorliegenden Diplomarbeit wurde das Problem der Bestimmung der Mischungshöhe unter Verhältnissen mit mechanisch angetriebener Turbulenz untersucht. Viele einfache diagnostische Gleichungen für die Bestimmung der Grenzschichthöhe enthalten den Coriolisparameter. Die wichtigsten Fragen dieser Studie sind die Leistung solcher diagnostischen Gleichungen in Gebieten nahe dem Äquator, wo der Coriolisparameter null ist, und die Relevanz des Coriolisparameters für die Bestimmung der Grenzschichthöhe. Für diesen Zweck wurde das numerische Modell “Weather Research and Forecasting Model (WRF)” verwendet. Numerische Simulationen wurden mit der idealisierten Ein-Säulen-Modellversion durchgeführt. Es wurde gezeigt, dass die einfachen diagnostischen Gleichungen in höheren Breiten gute Übereinstimmung mit dem Modell zeigen, aber nicht in der Lage sind, die Mischungshöhe in der Äquatornähe zu bestimmen. Es wurde weiters gezeigt, dass der Coriolisparameter für die Bestimmung der stabilen und neutralen Grenzschichthöhe weniger relevant ist als die Anfangsgeschwindigkeit des Windes, Schubspannungsgeschwindigkeit und die Brunt-Väisälä-Frequenz.

Declaration by candidate

I hereby state that this thesis does not contain material, which has been ever accepted for the award of any other degree or diploma in any University or other tertiary institution. As far as I know, this thesis does not contain any material which has been published before by other people, unless stated.

Numerical experiments described in this thesis were conducted by myself. Any help from other people is acknowledged. All figures were either made by myself as a result of numerical simulations or taken from sources which have been cited. To my knowledge, there are no intellectual property issues or conflicts of interest with other people or organizations with respect to the data presented in this thesis.

I give my permission to photocopy and lend this thesis after being deposited to the Library of Vienna University.

1. Introduction

1.1 Atmospheric boundary layer and definitions of atmospheric boundary layer height

The Earth's atmosphere receives the largest part of its energy from the Sun and transforms it into the movement of air masses. Flow in the atmospheric boundary layer is controlled by the diurnal cycle of the surface energy budget (Sorbjan, 1989):

$$R_n + G + H + E = 0 \tag{1}$$

where R_n is the flux of net radiation, G is the vertical heat flux in the soil, and H and E are the turbulent sensible and latent heat fluxes.

Interactions between the atmosphere and the surface take place in the atmospheric boundary layer. The atmospheric boundary layer (ABL) is the layer of fluid directly above the Earth's surface, in which significant fluxes of momentum, heat and/or moisture are carried by turbulent motions, whose circulation timescale is a few hours or less (Garratt, 1994). Another definition: Boundary layer (ABL, PBL, BL) is that part of the atmosphere that is directly influenced by the presence of the earth's surface, and responds to surface forcings with a timescale of about an hour or less (Stull, 1988). This lowest part of the atmosphere intensively exchanges heat, mass and momentum with the Earth's surface. The atmospheric boundary layer is of a great importance, both practical and scientific, because all human and biological activities take place in this part of the atmosphere: we actually live there.

Heat flux influences the vertical distribution of temperature in the boundary layer (Sorbjan, 1989). This temperature stratification can be classified into three categories: stable, unstable and neutral. In the case of stable stratification any particle moving vertically is impeded by buoyancy (for example, if a parcel of air is moving down, it is lighter than surrounding air and will be pushed upwards), which leads to suppression of turbulence and can even cause a laminar flow. In unstable stratification a vertically moving parcel of air is accelerated by buoyancy, which increases turbulence. In the neutral case there are no buoyancy forces. Stable cases usually occur at night, unstable during daylight hours, and neutral cases are observed during transitions between day and night or certain weather. Therefore, the structure of the boundary layer changes with time of the day (Figure 1), it is also dependent on weather and season. The depth of ABL is lower at night and in winter and higher at daytime and in summer and can range from tens of meters in case of strongly stable stratification to a few thousand meters in highly convective conditions. Apparently, a stable stratification will reduce mixing (and surface stress), and an unstable stratification will increase mixing.

In case of stable or neutral stratification the turbulent mixing is mechanically driven (Holton, 1979). The boundary layer is divided into several sublayers: the roughness sublayer, the surface layer and the outer boundary layer (Figure 2). In the roughness layer the profiles of wind and temperature are defined from roughness elements of the surface (for example, trees, fields, buildings and so on). In the inertial sublayer the wind profile practically does not rotate, whereas in the outer boundary layer the rotation of the Earth plays an important role and a characteristic rotation of the wind with the height takes place.

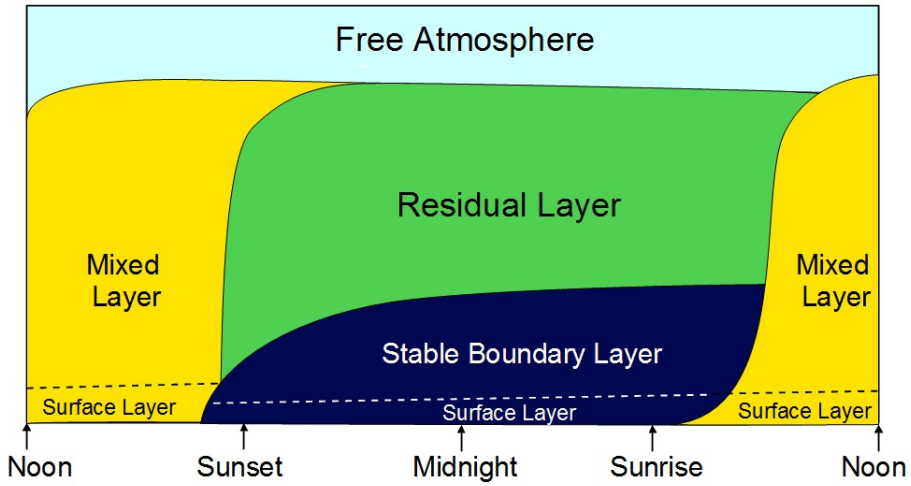

Figure 1: The structure and the diurnal cycle of the boundary layer. Source: `http://elte.prompt.hu`, originally from Stull (1988)

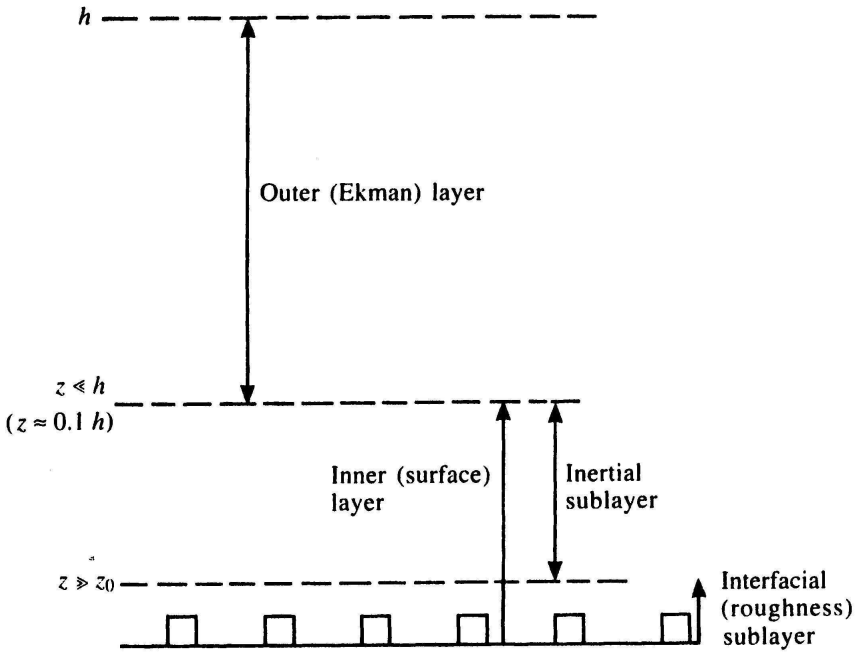

Figure 2: The structure of the boundary layer over a rough surface. The picture is taken from Garratt (1994)

.

The surface layer is defined as the lowest 10% of the total atmospheric boundary layer, and the outer boundary layer starts at the top of the surface layer and extends to a height of approximately 1 km. The outer boundary layer is characterised by a balance between the Coriolis force, the pressure gradient force, and the viscous stress (Figure 3).

As it has already been mentioned, studying the boundary layer is important both for practical and scientific reasons. It is of interest in meteorology, because the dynamics of boundary layer can predict the behavour of aerosols, water vapour and different pollutants. One of the fundamental parameters characterising the structure of the lower troposphere and a key parameter for air pollution models is the height of the atmosperic boundary layer, or the **mixing height**. Mixing

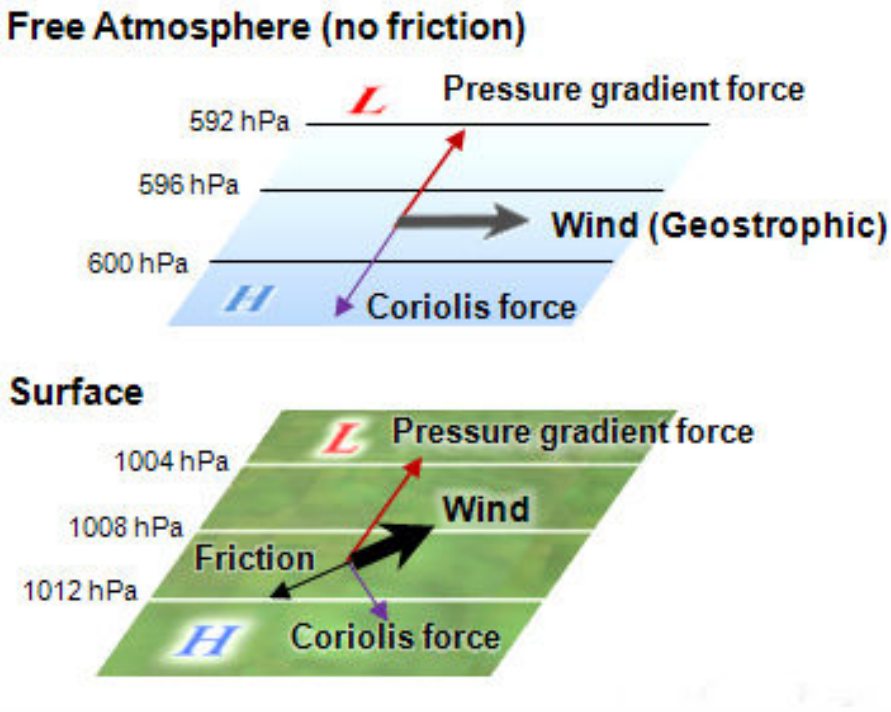

Figure 3: Balance of forces acting on air parcels near the surface and above the friction layer. Picture taken from `http://ftp.comet.ucar.edu`.

height (MH) is a key parameter in air pollution models determining the volume available for pollutants to dispersion (Seibert et al., 2000) and the structure of turbulence in the boundary layer (Hashmonay et al., 1991).

There are many definitions of mixing layer height used in different contexts. Seibert et al. (2000) proposed the following definition for the mixing layer height: The mixing height is the height of the layer adjacent to the ground over which pollutants or any constituents emitted within the layer or entrained into it become vertically dispersed by convection ar mechanical turbulence within a time scale of about an hour. The mixing layer coinsides with the atmospheric boundary layer, if the latter is defined as a turbulent domain of the atmospere adjacent to the ground (Seibert et al., 2000).

1.2 Methods for the determination of the mixing height

1.2.1 Overview of methods

Mixing height cannot be observed directly by standard measurements. Because the atmospheric boundary layer is a turbulent layer, an accurate mathematical theory for the structure of the velocity field in the layer is not possible. Methods for diagnosing the height of the boundary layer are based on identifying a feature in the vertical structure of an observable variable which robustly identifies the vertical extent of turbulent or thermal effects due to the surface (Sugiyama and Nasstrom, 1999). The success of any method depends on the availability and resolution of data (observations or numerical model output) and the atmospheric conditions. Even when data are available, the atmospheric boundary layer may contain complicated structures, (for example,

internal thermal boundary layers) which makes exact definition of the top of ABL difficult. A difficult problem is the determination of nocturnal boundary layer, as the height of the turbulent layer, the height of the nocturnal inversion, and the height of the wind maximum generally do not coincide. Further, the night-to-night variability is often greater than the variability during a single night and also boundary layer tends to flow to become decoupled from the surface (Garratt et al., 1996).

There are two basic possibilities for the practical determination of the mixing height (Seibert et al., 2000). One can derive it from profile data (measurements or model generated fields) and its parametererisation using simple equations or models (which only need a few measured input values).

Three primary observation methods are used to determine the mixing height: meteorological radiosondes, aeroplane surveys, and ground-based remote sensing (Tang et al., 2016). Radiosoundings are the most conventional source of data for determination of the MH.

Subjective methods of estimation of the MH include analysing radiosonde temperature and wind profiles in the lower part of the atmosphere. Under convective conditions, one could identify MH with the base of an elevated inversion or stable layer, or as the height where the air moisture reduces significantly, offen accompanied by wind shear (Seibert et al., 2000). Also, inversion base altitude increased by half of the depth of the inversion layer can also be taken as the characteristic CBL height (Stull, 1988).

The most important methods to determine objectively the boundary layer height are the following:

1. The parcel method

The parcel method (also called Holzworth method, (Holzworth, 1964)) is a standard Theta-based (potential temperature) method. Parcel methods can be used only in convective conditions, because the shear contribution is neglected. The Holzworth technique provides a relatively easy and reasonable determination of mixing height from temperature profile data (soundings and/or model-derived soundings). The basic idea of this method is to follow the dry adiabate starting at the surface with the measured or expected (maximum) temperature up to its intersection with the temperature profile from the most recent radiosounding. It determines the MH as the equilibrium level of a hypothetical rising parcel of air representing a thermal (Seibert et al., 2000). The method was improved by taking temperature advection, subsidence and other effects into account (Miller (1967),Garrett (1981)). However, this method depends heavily on the surface temperature, which can cause a high uncertainty in the MH estimation in cases when there is no pronounced inversion at the convective boundary layer top (Seibert et al., 2000). Also, the use of potential temperature θ (i.e., a dry atmosphere assumption) causes height underestimations (Fearon et al., 2015).

2. Bulk Richardson number methods

The bulk Richardson number is defined as

$$Ri_b(z) = \frac{g(z - z_0)(\theta(z) - \theta(z_0)}{\theta(z)(u(z)^2 + v(z)^2)}, \tag{2}$$

where g is the gravity acceleration, z_0 is the altitude of the measurement location above sea level, θ is the potential temperature, and $u(z)$ and $v(z)$ the wind zonal and meridional components, respectively. The MH is defined as the height where the bulk Richardson number equals the critical Richardson number of 0.21 [Seibert et al., 2000]. At heights where Ri_b is higher than this thresh-

old value (which is called “the bulk Richardson number for the entire ABL”), the atmosphere is considered to be free of turbulence (free troposphere). Unfortunately, the MH estimates based on standard radiosondedata can result in quite high uncertainty because of coarse resolution. Particular problems occur under stable atmospheric conditions since no universal relationships seem to exist between the profiles of temperature, humidity or wind (Feng et al., 2015).

There is a large number of observation stations, which conduct meteorological radiosonde ascents. These stations are distributed all over the globe and provide reliable data. However, due to high costs of the observation, most stations make only two observations at 00:00 and 12:00 UTC (Seibert et al., 2000). When solar radiation increases in the morning, the growth rate of the MH reaches hundreds of metres per hour, which leads to a quick development of convection. Even if hourly observations were available, they could not provide sufficient temporal resolution of the evolution of MH, it would still be impossible to study its time evolution (Seibert et al., 2000). Aeroplane surveys can be used to obtain high-resolution meteorological and pollutant profiles, but because of weather conditions, air traffic control and observation costs these data are limited to short time periods. Therefore, to acquire continuous observations with high spatial and temporal resolution, ground-based remote sensing has become the most advanced approach to MH measurement.

1.2.2 Remote-sensing-based methods

Sodar (acoustic radar), lidar (laser radar) and Doppler radar (electromagnetic radar) are the three ground-based remote sensing methods. The mixing layer has a much higher concentration of water vapor and aerosols in comparison with the free atmosphere. The decrease in water wapor and aerosols is abrupt, which causes a sharp lidar signal change (around the top of the boundary layer. Lidars can obtain the vertical profile of the aerosol concentration. For that reasons lidars can be used to detect the temporal and spatial variations in the MH over different areas (Kunkel et al. (1977), Boers et al. (1984), Melfi et al. (1985)). Thus, a lidar is able to derive the atmospheric MH by calculating the height at which sudden changes in the profile occur. Ceilometers are a relatively new remote-sensing device. A ceilometer is a single-wavelength, eye-safe backscatter lidar, which also measures aerosol concentration profile. Both conventional lidars and ceilometers measure laser light backscattering, which enables to determine the attenuated backscatter coefficient the aerosol backscatter coefficient could be also retrieved (Klett, 1981). Through the following calculation of backscatter coefficient a cloud base (for which the ceilometers were originally designed) and also the ABL height can be obtained Eresmaa et al. (2006). The difference between ceilometer and lidar is that ceilometer has a less powerful, but a spectrally broader laser. The ability of ceilometers to detect aerosols is limited up to around 3 km height (Markowicz et al., 2008), which is less than the height detected by lidars, but the ceilometers offer some advantages: they have lower operational and maintenance cost, are relatively easy to operate and data from them are available in near-real time (Wiegner et al., 2014).

A sodar can obtain the vertical profiles of wind and temperature, which can be used to estimate the MH. A Doppler wind radar gets variations of the wind vectors at different altitudes and identify the mixing layer through wind shear. Sodar, wind-temperature radar and ceilometer can be combined to derive MH (Clifford et al., 1994). These three instruments deliver five types of vertical profiles: wind and acoustic backscatter from the SODAR (Sound detection and ranging) instrument, wind, temperature and electromagnetic backscatter from the WTR (Wind-temperature-radar) instrument, and optical backscatter from the ceilometer (Feng et al., 2015).

In their reviews Beyrich (1997), Seibert et al. (2000) and Emeis et al. (2008) compared advantages and disadvantages of acoustic radar (sodar), laser radar (lidar) and electromagnetic radar (Doppler radar) methods. The profiles mentioned above have to satisfy the following criteria (Seibert et al., 2000):

- They should cover the layer between the earth's surface and up to 3 km above ground, because this is the range, in which MH varies with day/nighttime and season
- The profile measurements should be updated one or more times per hour, otherwise the description of MH evolution would be impossible
- The measured profiles must have a vertical resolution of about 10-30 m to avoid relative uncertainties of more than 10-20%, especially for low mixing heights (lower than 250 m)
- The measured parameters should be linked physically to the vertical mixing of pollutants

The sodar detection height is usually less than 1000 m, which is not enough for observing the MH of convective boundary layer. The lowest detection height of wind radar is normally above 200 m (that means, not from the ground), and its vertical resolution is limited to 50–250 m, which creates uncertainties. These uncertainties make the interpretation of wind radar data not always straightforward (Seibert et al., 2000). Before the use of ceilometers was started, lidar was costly and not widely used. In recent years, lidar observation technology has developed rapidly, and it has been used for MH observations in increasing number of applications. Meanwhile, eye-safe ceilometers that permit observation of the MH with a near infrared band laser have been developed (Tang et al., 2016). Due to their simple operation and low cost, these instruments have become the optimal and widely used method for MH observation recent years (Münkel and Räsänen, 2004). However, a combination of different systems and methods is still preferable for a successful MH determination.

Even though a noticeable progress has been made in improving profile measurements techniques, they are still not widespread and reliable enough to provide the necessary data. This is why simple parametrisations based on standard surface observations (diagnostic or prognostic equations) are still widely used.

1.2.3 Methods using surface data and parametrisation

A lot of parametrisation expressions for the height of the turbulent stable boundary layer (SBL) have been suggested in the literature. Burzynski et al. (2004), who compared mixing height values generated by a pre-processor with with a monostatic sodar measurement, list eight of them in their conference paper (Table 1).

We will return to some of the equations listed in Table 1 in Chapter 3.

The most popular diagnostic equations based on scaling arguments are the following (Seibert et al., 2000):

neutral

$$h = a_1 L_E = a_1 u_* / f \tag{3}$$

Table 1: Some diagnostic equations for the calculation of mixing height. PGT means Pasquill atmospheric stability classes: D is neutral, E slightly stable and F stable. Source: Burzynski et al. (2004)

Reference	Mixing height equation	Range of use (PGT)	Correlation coefficient	Mean values [m]	Standard deviation [m]
1.Arya (1981) (after Zilitinkevich, 1972)	$h = a\left(\frac{u_* L}{f}\right)^{1/2} + b;$ $a = 0.43, b = 29.3$	D-F	0.138	150.7	130
2.Zilitinkevich (1972)	$h = c_2\left(\frac{u_* L}{f}\right)^{1/2},$ $c_2 \approx 0.4 \ (0.13 \div 0.72)$	E,F	0.138	115.6	130.6
3. Arya (1981)	$h = 0.089\frac{u_*}{f} + 85.1$	D-F	0.178	179	62.5
4. Mahrt (1982)	$h = 0.06\frac{u_*}{f}$	D-F	0.178	63.4	42
5.Nieuwstadt (1984)	$h = 28u_{10}^{3/2}$	D-F	0.298	60.3	35
6. Benkley & Schulman (1979)	$h = 125u_{10}$	D-F	0.31	200.8	78.4
7. H van Dop	$h = 0.263L\left[\left(1+\left(2.28\frac{u_*}{fL}\right)\right)^{1/2} - 1\right]$	E-F	0.135	65.6	76.5
8. Dierdorff	$h = \left[\frac{1}{30L} + \frac{f}{0.4u_*}\right]^{-1}$	D-F	0.173	262.5	194.5

Where: h- mixing height; u - wind speed (10m); f - Coriolis parameter, u_* roughness wind speed; L – Monin – Obukhov Length. The mean value for the mixing height in the sodar data set equals to 364.7 m with standard deviation 137.5 m

.

and stable

$$h = a_2(L_E L_*)^{1/2} = \frac{a_2 u_*^2}{\sqrt{-\beta\kappa Q_0 f}}, \tag{4}$$

where u_0 is the friction velocity, $a_1 = 0.07 - 0.3$ and $a_2 = 0.3 - 0.7$ are empirical coefficients, f is the Coriolis parameter, Q_0 is the surface heat flux, $L_E = u_*/f$ und $L_* = u_*^3/\beta\kappa Q_0$ are Ekman and Monin-Obukhov length scales. Equation 3 assumes a neutral, stationary boundary layer.

Nieuwstadt (1981) proposed a combination of 3 and 4:

$$h = \frac{L_*}{3.8}\left(-1 + \sqrt{1 + 2.28\frac{u_*}{fL_*}}\right) \tag{5}$$

Most of the verification studies done in the past show that more elaborated parameterisations than Equation 5 do not show good agreement with the observations (see, for example, Table 1) Also, Coriolis force may play only a subordinate role for the turbulent fluxes (Andren, 1995).

Burzynski et al. (2004) state that some of the parameterisations can be a little bit improved, but promising tools can be formulae including the Brunt-Väisälä frequency

$$N = \sqrt{\frac{g}{\theta}\frac{\partial\theta}{\partial z}} \tag{6}$$

where N represents the background stratification at the top of the ABL (Joffre et al., 2001). Unfortunately, for the calculation of N the vertical profile of temperature is needed, up to heights above the top of the ABL. This is limiting the application of that method.

Zilitinkevich and Mironov (1996) proposed a diagnostic equation where the mixing height h is governed by three key physical processes: rotation of Earth (given by the Coriolis parameter), surface buoyancy flux ($B_s = (g/\theta)\overline{w\theta_s}$) and free-flow stability (Brunt-Väisälä frequency).

$$\left(\frac{fh}{C_n u_*}\right)^2 + \frac{h}{C_s L^*} + \frac{Nh}{C_i u_*} = 1 \tag{7}$$

In the equation, L^* is the modified Obukhov length $L^* = -u_*^3/B_s$, and C_n, C_s, C_i are constants of proportionality. The main advantage of this equation is that, unlike the equations above, it remains defined for $N \to 0$, $L_* \to \infty$ and, what is more important for us, $f \to 0$.

The same authors improve their equation 7 by adding two additional terms to "include the cross interactions" between the first three terms, and the equation takes a form:

$$\left(\frac{fh}{C_n u_*}\right)^2 + \frac{h}{C_s L^*} + \frac{Nh}{C_i u_*} + \frac{\sqrt{|fB_s|h}}{C_{cr} u_*} + \frac{\sqrt{|fN|h}}{C_{ir} u_*} = 1 \tag{8}$$

Here C_n, C_n,C_n, C_n, C_n are constants that were given by Zilitinkevich and Mironov (1996), but then also reevaluated by many other authors, yielding a wide range of these constants, which is a problem of this equation.

Steeneveld et al. (2006) evaluate the performance of equations 7 and 8. They come to conclusion that the model based on equations underestimates the mixing height. Steeneveld et al. (2006) also question the relevance of the Coriolis parameter for this estimation. We will return to this important paper in Section 1.3.

There are also prognostic equations for describing the stable boundary layer height are based on a relaxation process, during which h approaches an equilibrium value h_e with a time scale t_s (Seibert et al., 2000):

$$\frac{dh}{dt} = \frac{h_e - h}{t_s} \tag{9}$$

Although it could be expected that prognostic equations would show better correspondence with the observational data, comparisons of different diagnostic and prognostic equations do not show that. Such data comparisons were performed by, for example, by Zilitinkevich et al. (2002).

As for convective boundary layer, diagnostic equations to parametrise the convective boundary layer height based on simularity theory were proposed by, for example, byTennekes (1970), Zilitinkevich (1972), San José and Casanova (1988) . These are valid only under certain conditions

(Seibert et al., 2000). Vogelezang and Holtslag (1996) used their Ri-method also for unstable conditions adding an excess temperature to the near-surface temperature.

Prognostic equations which predict the growth of convective boundary layer are normally derived from a parameterisation of the TKE budget equation (see Section 1.4 below) which is either averaged over the whole mixed layer or specified at the mixed layer top (Seibert et al., 2000). Prognostic equations were suggested by many scientists, the earliest by Lilly (1968). The equations proposed by different scientists differ mainly in a way they neglect certain terms in the TKE budget and parameterise the remaining terms. Most recent analytical solutions for the prognostic equations for a diurnal convective boundary layer were proposed and evaluated by Ouwersloot and Vilà-Guerau de Arellano (2013).

In the present diploma thesis we will derive this height from profile data obtained from the output of WRF model simulations based on a Mellor–Yamada–Janjiċ parameterisation scheme (see in the chapter “WRF model” below). With the help of these simulations we are going to contribute to solving a problem of the Coriolis parameter and scale $1/f$ for mechanicaly driven, near-neutral ABL. The main question is: can we reproduce mixing layer height h as a function of latitude and the Coriolis parameter ($h(\phi) \sim f(\phi)^{-1}$ when $f \to 0$?

1.3 The Coriolis parameter in diagnostic equations and parameterisation schemes

In mechanics, Coriolis force is defined as an inertial or fictitious force that seems to act on objects (for example, air parcels) that are in motion within a frame of reference that rotates with respect to an inertial frame. We can explain its action with the following simple example: we take a horisontal disc with the center O and we draw a radius OA. Let a small ball roll along the radius OA with the velocity $\vec{v}$. When the disk is at rest, the ball continues moving aong OA, but when it is rotating with an angular velocity $\vec{\omega}$, the ball takes the trajectory OB (Figure 4). That means that in relation to non-inertial reference frame "rotating disk" the ball behaves so, as if a force

$$\vec{F}_c = 2m\vec{v} \times \vec{\omega} \tag{10}$$

was acting on it. As we see from equation 10, Coriolis force $\vec{F}_c$ is a cross product of two vectors, $\vec{v}$ and $\vec{\omega}$.

Figure 4: Rotating disc (left), Coriolis force acting on objects that move along the meridian (right). Source: `http://ens.tpu.ru`.

It is well known that Coriolis force: 1) deflects the wind to the left in the Southern Hemisphere and to the right in Northern Hemisphere (Figure 4) 2) is strongest at the poles and zero at the equator 3) is proportional to the wind speed 4) cannot start a wind and cannot do work.

Deflection of an object due to the Coriolis force is called the Coriolis effect.

The Earth is a rotating frame, and the Coriolis deflection is related to the motion of the object, the motion of the Earth, and the latitude. It takes the Earth one so called sidereal day to make a full revolution. A sidereal day is approximately 86164 seconds, or 23 hours, 56 minutes 4.091 seconds (`http://hpiers.obspm.fr/eop-pc/models/constants.html`). We name it a sidereal rotation period T_s and calculate an angular rotation rate (Stull, 2016):

$$\Omega = 2\pi/T_s = 0.7292116 \cdot 10^{-4} \mathrm{s}^{-1} \tag{11}$$

The Coriolis parameter is then defined as follows:

$$f = 2\Omega \sin\phi \tag{12}$$

where ϕ is the latitude (Figure 5), and $2 \cdot \Omega = 1.458423 \times 10^{-4}$ s^{-1}. The physical meaning of Coriolis parameter is calculation of the horizontal component of the Coriolis force caused by horizontal movements. From the equation 12 it is clear, that the Coriolis parameter depends only on latitude (Figure 6).

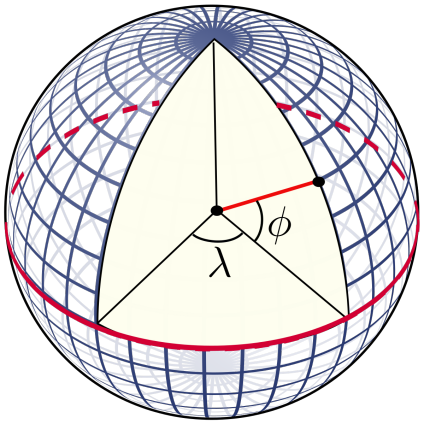

Figure 5: Definition of geographical latitude and longitude.

Looking at the equations 3 to 5 and equations by Arya (1981) and Mahrt et al. (1982) in Table 1, one may notice that in stable conditions mixing height h is indirectly proportional to the Coriolis parameter f. When defined by these equations, how would it behave in the equator area where the Coriolis parameter is zero (Figure 6)?

Figure 7 shows mixing height as a function of latitude calculated with the equation 3 where the friction velocity $u_* = 0.33$ m/s and the empirical coefficient $a_1 = 0.3$. One can easily see the unrealistic increase of mixing height in the equator area.

There are not so many research works on this topic, may be because of the problem of finding a diagnostic equation for mixing height is relevant mostly for stable boundary layer and not for convective. Obtaining the daytime convective boundary layer height from profile observations is straightforward (e.g., Vogelezang and Holtslag, 1996, Seibert et al., 2000). Studying a similar problem in oceanography (finding an explicit expression of bounday layer height) is not produc-

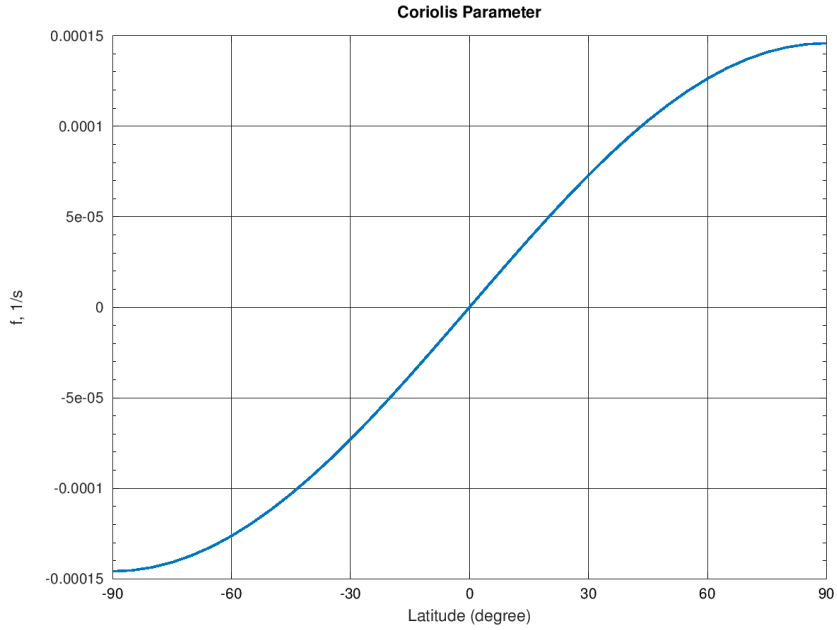

Figure 6: Variation of the Coriolis parameter with latitude.

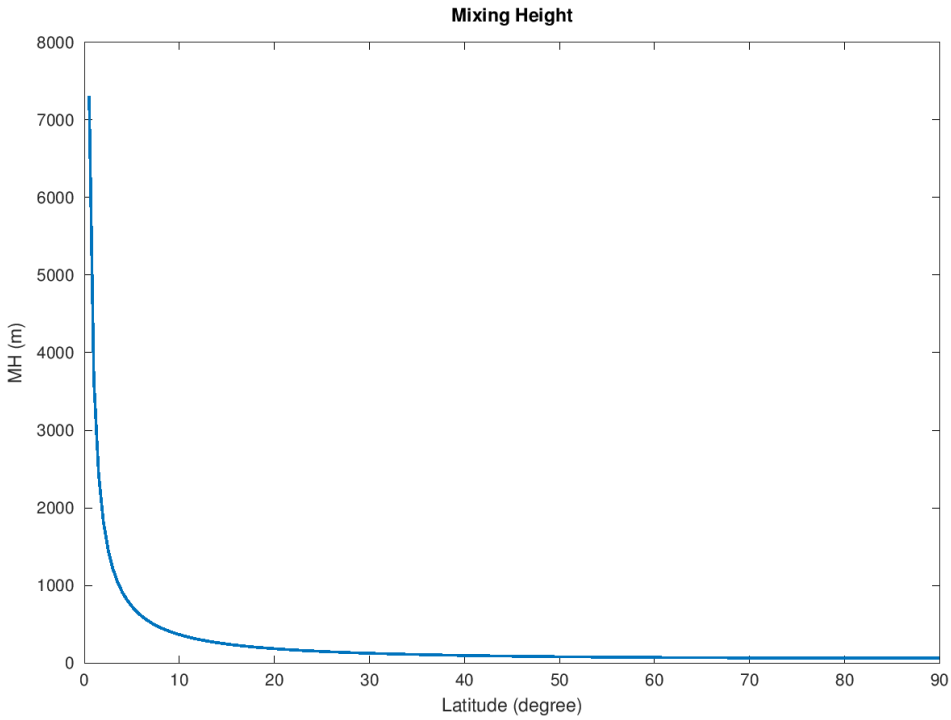

Figure 7: Mixing height as a function of latitude as described by Equation 3, u_*=0.33 m/s, a=0.3.

tive, because the boundary layer height in the ocean can be easily defined through observed temperature profiles, which is describen in numerous papers (for example, Kara et al., 2000). For stable boundary layer (especially for very stable conditions), however, observational value of mixing height can be distorted by suppressed turbulence (Holtslag and Nieuwstadt, 1986, Vickers and Mahrt, 2004), as well as radiation divergence (Garratt and Brost, 1981), gravity waves, wave breaking (Newsom and Banta, 2003) and baroclinicity (Zilitinkevich and Esau, 2003). Also, as

Table 2: Correlation coefficient r between the relevant quantities and the FPC. Source: Steeneveld et al. (2006)

Parameter	r
u_*	0.75
N	0.47
$\overline{w\theta}$	0.37
f	0.15
z_0	0.16

it has already been mentioned in Chapter 1, there are problems of interpretation of wind and temperature profiles for SBL.

The Coriolis parameter f in relation to mixing height for stable boundary layer is mentioned in Steeneveld et al. (2006). This paper evaluates diagnostic equations 7 and 8 against four observational data sets and large-eddy model simulations. Table 2 shows the absolute values of correlation coefficients between observed friction velocity u_*, free flow stability N (Brunt-Väisälä frequency), turbulent flux $\overline{w\theta}$, f and roughness length z_0, and the values of first principal components (FPC) obtained by principal component analysis, which was performed on the observed mixing height. This analysis is performed over all the datasets used in the research (3 observational datasets and a LES model output). All these are relevant variables that govern h. As seen in the table, the Coriolis parameter has a correlation coefficient of only 0.15. The authors raise a question, which is important for us: is Coriolis force (as well as roughness lengh z_0) a relevant parameter for estimating the mixing height in stable conditions? To answer this question, they omit the Coriolis parameter and distinguish two regimes: for moderately stable conditions h is proportional to u_0/N, and for strongly stable conditions to the length scale $(|B_s|/N^3)^{1/2}$ where B_s is surface buoyancy flux. Finally, the authors determine that the strongest relation of h exists with the friction velocity u_* and with N, while the Coriolis parameter f is less important. In the article they use only observational datasets in regions far from equator: CASES-99 in Kansas, observatory of Sodankylä, Lapland, in Netherlands and in the Arctic (SHEBA). LES simulations were also performed over the Arctic region. The question of bias between observational data in the near-equatorial regions and values yielded by diagnostic equations with or without the Coriolis parameter is therefore still open.

Syrakov (2015) proposes a general theoretical formula for the boundary layer height h. This new analytic formula is obtained through integration and parametrisation of the TKE equation 19. He distinguishes the cases with stable/neutral and unstable stratification and also consideres separately the case when the Coriolis effect is neglected. The author notes that the equation for the latter case, as well as its limit cases, has still to be analysed. The equation itself has many parameters, description of those is beyond the scope of this study. For the constants used in this equation further experimental studies are needed, because at the moment the equation has the same problem with its constants of proportionality as equation 7 cited in the Introduction: in both equations the constants have a very wide range and a lot of work is being done to indicate values for them.

Samah (1997) states that in the equatorial boundary layer the Coriolis parameter is small or zero and moisture plays a more important role in the control of stability and the surface energy balance than it does in the midlatitude boundary layer. Samah employed the meteorological preprocessor OML (Olesen et al., 1992). The preprocessor uses a set of prognostic equations for

the convective boundary layer derived by Tennekes (1973) and Tennekes and Drierdonks (1981) improved by Stull (1983). Samah (1997) made a small change to the set of equations in which the potential temperature was replaced with virtual potential temperature to include the effects of moisture. The model output was compared with radiosonde observations in Kuala Lampur and in Rondonia, Brazil. The radiosonde observations showed that the stability of the boundary layer and such parameters as energy flux and mixing height were strongly influenced by moist processes. The model yielded data with a big discrepancy to the observed data: the author notes that current scheme needs to be improved to include some measure of moisture stratification. But he does not mention the Coriolis parameter any more, which leaves the question about its influence unanswered. A logical conclusion is that this parameter is of a small importance in comparison with the moisture.

As we see, the the problem of estimating the mixing height in equatorial regions coupled with the problem of Coriolis coefficient still needs further research.

1.4 Closure schemes and turbulent kinetic energy

For the forecasting and study of weather, climate and air quality basic equations governing atmospheric behavior are solved numerically. These equations are the equation of state, the equation of continuity (mass), the first law of thermodynamics (heat), the conservation equations of momentum (Navier-Stokes equations) and equations expressing the conservation of moisture, trace gases and air pollutants. The governing equations have to be integrated. The equations are nonlinear and after Reynolds averaging contain more variables than the number of equations, and to solve the system, we need to find new equations that relate the turbulent fluxes to the mean quantities, for which we already have equations (Blackadar, 1998). K-theory is a class of boundary layer parametrisations for eddy-diffusivity models. The symbol for eddy diffusivity (see equation 16 below) is often K (in the equation 16 K_c), hence this theory is called K-theory. K-theory encompasses (Garratt, 1994):

- local first-order closure: K is specified from the vertical and static stability.
- 1.5-order (TKE) closure: TKE (turbulent kinetic energy) is predicted with a prognostic equation, and K is specified using the TKE and some lengthscale
- K-profile approaches: A specified profile of K is applied over a diagnosed turbulent layer depth based on surface fluxes or other vertically-aggregated forcings for turbulence.

One of the common solutions is the first order closure. It is called “first-order”, because only equations of the first moment (mean) quantities remain when the closure is complete. Let’s say C is an atmospheric variable. Then a budget equation in general form looks like

$$\frac{\mathrm{d}C}{\mathrm{d}t} = S \tag{13}$$

In the equation S is the summation of sources and sinks for the variable C, and $\mathrm{d}C/\mathrm{d}t$ is the total rate of change for this variable. Then, if density is constant, a budget equation has a following form (Holtslag and Steeneveld, 2011):

$$\frac{\partial C}{\partial D} + u\frac{\partial C}{\partial x} + v\frac{\partial C}{\partial y} + w\frac{\partial C}{\partial z} = S \tag{14}$$

We can separate mean and turbulent parts (local, instantaneous values) of the flow using the method of Reynolds averaging (described, for example, in Blackadar, 1998). Reynolds separated each of the velocity components, which we denote by u, v, and w, into two parts: mean value $\overline{u}$, $\overline{v}$ and $\overline{w}$, and a turbulent deviation u', w' and w' associated with turbulent eddies.

Our variable C can be represented as $C = \overline{C} + c'$ where $\overline{C}$ is a mean value of C, and c' is an instantaneous value. After Reynolds averaging, some algebraic modifications and simplifying assumptions, a budget equation for the mean variable $\overline{C}$ takes a form:

$$\frac{\mathrm{d}C}{\mathrm{d}t} = \frac{\partial C}{\partial t} + \overline{U}\frac{\partial \overline{C}}{\partial x} + \overline{V}\frac{\partial \overline{C}}{\partial y} + \overline{W}\frac{\partial \overline{C}}{\partial z} = \overline{S(C)} - \frac{\partial \overline{u'c'}}{\partial x} - \frac{\partial \overline{v'c'}}{\partial y} - \frac{\partial \overline{w'c'}}{\partial z}. \tag{15}$$

To solve such an equation, the terms involving turbulent fluxes have to be parametrised: the fluxes need to be expressed in terms of available mean model quantities. After that the equations can be integrated: starting with initial values, new values are calculated with each time step.

In the K-theory it is assumed that the flux $\overline{w'c'}$ of a variable C in the vertical direction z is down the vertical gradient of the mean concentration of C per unit mass:

$$\overline{w'c'} = -K_c \frac{\partial \overline{C}}{\partial z} \tag{16}$$

In the equation, K_c is an "eddy-diffusivity", or mixing coefficient for the variable C, which has a dimension length scale l. One possible parametrisation is:

$$K_c = l^2 S f(Ri) \tag{17}$$

In this diagnostic equation S is vertical wind shear and Ri is the Richardson number. The equation shows that eddy-diffusivity K_C changes with wind speed, height, stability and other parameters. If we relate the eddy diffusivity of Equation 16 to the actual turbulent kinetic energy of the flow, we can develop a prognostic approach to solving the equations. We can do it by using the prognostic turbulent kinetic energy equation and an appropriate choice for the turbulent length scale. Turbulent kinetic energy is a measure of turbulence: the value of turbulent kinetic energy (TKE) directly represents the 'strength' of the turbulence in the flow. The concept of turbulent kinetic energy is very similar to the idea of kinetic energy and is defined as the sum of the squared velocity fluctuations:

$$\overline{e} = \frac{1}{2}\left(\overline{u'^2} + \overline{v'^2} + \overline{w'^2}\right) \tag{18}$$

The prognostic equation for TKE (or e) in its basic form is as follows:

$$\frac{\partial e}{\partial t} = -\overline{uw}\frac{\partial \overline{U}}{\partial z} - \overline{vw}\frac{\partial \overline{V}}{\partial z} + \frac{g}{\overline{\Theta_v}}\overline{w\theta_v} + D - \epsilon \tag{19}$$

The expression on the left side means the local variation of e (TKE) with time. Advection is not considered. The first and the second term at the right represent the shear production of turbulence, and these terms are normally positive (Figure 8). The third term on the right side describes production or destructive loss of turbulence by buoyancy effects. Here there are two cases possible: if the boundary layer is unstable (mean potential temperature decreases with

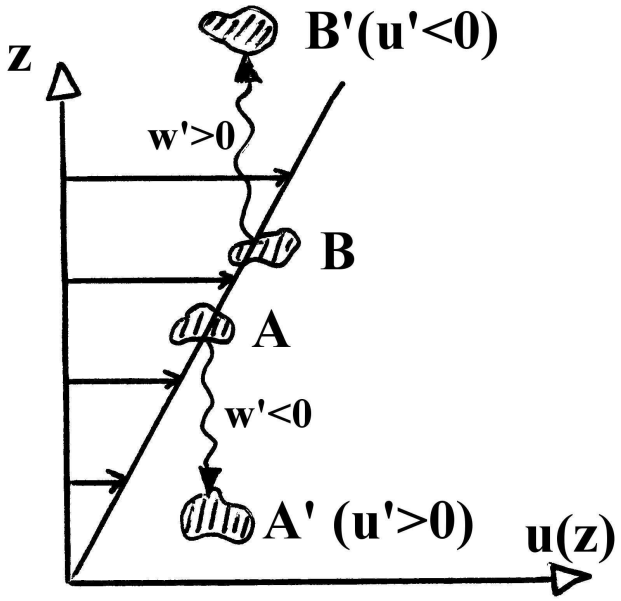

Figure 8: Shear production of turbulence. The figure was taken from `http://www.iac.ethz.ch`, author: M. Spengler.

the height), the TKE produced, because its source term, which depends on the virtial potential temperature $\overline{\Theta_v}$ and its turbulent flux $\overline{w\theta_v}$, is then positive. The situation is different with a stable boundary layer where the potential temperature increases with height, which causes destructive loss of TKE. The term D represents divergence and pressure redistribustion terms: transport of TKE through the turbulent fluxes and work of pressure forces. ϵ is molecular dissipation of TKE into heat and it is always positive. Mostly the smallest eddies are responsible for this dissipation. During the day this term reaches its maximum near the surface and stays nearly constant in the mixed layer. At the heights above the mixed layer this value declines and is practically zero at the point of reaching free troposphere. At night the dissipation rapidly decreases with height.

With the equation 19 TKE can be calculated for given mean profiles, and corresponding fluxes are derived from equation 16. An approach known as "TKE-length scale approach" can be developed, in which the diffisivities are calculated with equations of the form:

$$K_c = \alpha_c l \sqrt{e} \tag{20}$$

This is an example of so-called 1.5 order closure.

One can theoretically derive equations for the rate of change of second-order statistics (fluxes), but these equations will contain new variables, third moments, and if you derive equations for them, then fourth order moments appear and so on (Blackadar, 1998). That is why there is no straightforward way to close the set of atmospheric equations without making hypotheses of these relations.

At the same time, when the TKE balance equation is a part of the equation system, TKE is one of the variables and therefore can be obtained as an output variable and visualised. The mixing

height can be estimated with the help of this visualisation, or by an algorithm of the WRF-model, and we use the value diagnosed in this way.

2. Method for studying ABL height behaviour

In the present diploma thesis we derive the mixing height from the output of WRF model simulations. With the help of these simulations we study the problem of influence of the Coriolis parameter and the scale $1/f$ on mechanically driven, near-neutral ABLs. The main question is: can we reproduce the behaavour of widely-used parametrisations of mixing layer height h as a function of latitude and the Coriolis parameter which contain the proportionality $h(\phi) \sim f^{-1}(\phi)$), especially in low latitudes when $f \to 0$?

2.1 WRF Model

The Weather Research and Forecasting (WRF) is an atmospheric model developed for both research and operational applications which be used for simulations across varying spatial scales from a few km to thousands of km. The model was developed as a collaborative effort of various institutions, for example, the National Centre for Atmospheric Research (NCAR), the National Centers for Environmental Prediction (NCEP), the National Oceanic and Atmospheric Administration (NOAA), the Forecast Systems Laboratory (FSL) and the Air Force Weather Agency (AFWA) (Skamarock et al., 2008). WRF is a supported "community model", which means that as a resourse WRF is free and can be shared: it has a distributed development, but a centralized suport (NCAR). WRF model was initially released in 2000 and since that it has become one of the most widely used numerical weather prediction models. The cumulative number of WRF registrations is now over 36,000 distributed across 162 countries, and this number continues to grow (Powers et al., 2017). Using WRF, one can carry out atmospheric simulations. The process has two phases:
1) configuring the model domain(s), ingesting the input data, and preparing the initial conditions
2) running the forecast model.
The forecast model components operate within WRF's software framework, which handles I/O and parallel-computing communications. WRF is written mostly in Fortran, can be built with a number of compilers, and runs primarily on platforms with UNIX-like operating systems (for example, Linux Debian, as in the present thesis), from laptops to supercomputers. For many cases the model can be run on one's home laptop after downloading the software from the internet site and compiling the model.

WRF has two dynamical cores: The Advanced Research WRF (ARW) and Nonhydrostatic Mesoscale Model (NMM). Both are Eulerian mass dynamical cores with terrain-following vertical coordinates A dynamical core includes mostly advection, pressure gradient force, Coriolis force, buoyancy force, filters, diffusion, and timestepping. Both are downloadable in the same WRF tar file (see, for example, WRF User Guide[1]). Physics, the software framework, and parts of data pre- and post-processing are shared between the dynamical cores. We are using ARW, which is a common choice for research applications, and all the following information concerns this core.

The governing equations for the ARW dynamics solver are the compressible, nonhydrostatic Euler equations. The details about the equations and variables can be found in, for example, in Skamarock et al. (2008).

[1] http://www2.mmm.ucar.edu/wrf/users/docs/user_guide_V3/contents.html

The initial conditions for the real-data cases are pre-processed through a separate package: WRF Preprocessing System. WRF simulations begin with this Preprocessing System (WPS), which first reads geographical information to set up the user's model domains. WPS is outside of the ARW system. The output from WPS is passed to the real-data pre-processor in the ARW, which then ingests, reformats, and interpolates the requisite first-guess atmospheric data (e.g., a global analysis or model forecast) to the user's domains. Finally, the input fields are put on the model's vertical levels and lateral boundary conditions are generated. WRF is then ready to run. This is done by the forecast component that contains the dynamical solver and physics packages for atmospheric processes (e.g., microphysics, radiation, planetary boundary layer, Figure 9).

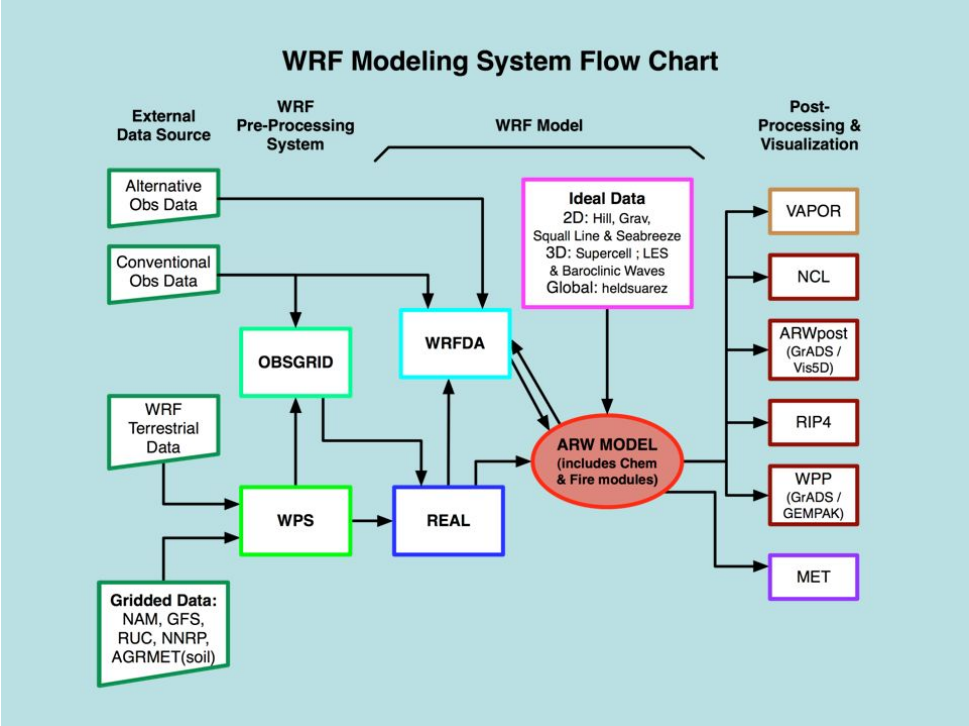

Figure 9: Flowchart for the WRF Modeling System, Version 3. Skamarock, 2017.

.

We can summarise the steps of WRF process as follows (Figure 9):

- WRF Pre-processing System :
  - Real-data interpolation for NWP runs (WPS).
  - Program for adding more observations to analysis (obsgrid).
- WRF Model (ARW and NMM dynamical cores) :
  - Initialization programs for real and (for ARW) idealized data (real.exe/ideal.exe).
  - Numerical integration program (wrf.exe) (WPS).

For research purposes WRF can be configured to conduct idealized simulations (Figure 10). This capability allows users to study processes in a simplified setting (e.g., reflecting a single sounding or idealized topography) by varying parameters and initial conditions while using limited physics. Skamarock, 2017 lists the following reasons for providing 12 idealised cases in WRF:

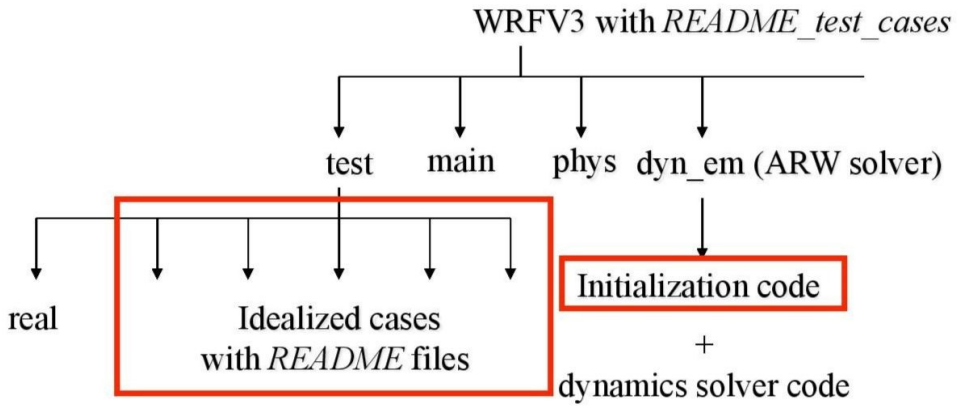

Figure 10: Idealised cases, more information. Flowchart author: Bill Skamarock, taken from `http://funnel.sfsu.edu/students/luyilin/Lu_Yilin/wrf/WRF_ideal_init_201401.pdf`

.

1. The cases provide simple tests of the dynamics solver for a broad range of space and time scale.
2. The test cases reproduce known solutions (analytic, converged, or otherwise).
3. The cases provide a starting point for other idealized experiments.
4. They can be used to test physics development.
5. These tests are the easiest way to test the solver.

The available 12 test cases are (information is taken from the general model description, a readme file):

1. 2D squall line (x)

   2D squall line (x,z) using Kessler microphysics and a fixed 300 m^2/s viscosity. A periodicity condition used in y, so that 3D model produces 2D simulation. The velocity component v should be zero and there should be no variation in y in the results. A number of detailed descriptions on how to run this case can be found in Internet, for example, a presentation for students by Chen (2014).

2. 2D squall line (y)

   Same as 2D squall line (x), except with (x) rotated to (y). u velocity should be zero and there should be no variation in x in the results.

3. 3D quarter-circle shear supercell simulation

   Left and right moving supercells are produced.

4. 2D flow over a bell-shaped hill (x,z)

   The case has the following parameters: 10 km half-width, 2 km grid-length, 100 m high hill, 10 m/s flow, N=0.01 s^{-1}, 30 km high domain, 80 levels, open radiative boundaries, absorbing

upper boundary. The case is in linear hydrostatic regime, so vertically tilted waves with 6 km vertical wavelength. One of the examples is shown in Chen (2014) mentioned above.

5. 3D baroclinic waves

   Baroclinically unstable jet u(y,z) on an f-plane. Symmetric north and south, periodic east and west boundaries. 100 km grid size 16 km top with 4 km damping layer. 41x81 points in (x,y), 64 layers. An example "baroclinic wave in a channel" is given in Skamarock (2017).

6. 2D gravity current

   Test case is described in Straka et al. (1993).

7. 3D large-eddy simulation

   A large-eddy simulation (LES) of a free convective boundary layer (CBL) without large-scale wind at the initial time, and the turbulence of the free CBL driven/maintained by the specified surface heat flux. An example is given in Skamarock (2017).

8. 2D full physics seabreeze

   The case is more set up now to demonstrate how to set all land variables so that full physics options may be used. Tuning is needed to produce real sea-breeze simulation at this point.

9. 3D global case

   A coarse-resolution global forecast case that is described in Held and Suarez (1994). This test of the global solver is dry, and produces midlatitude jets, breaking midlatitude baroclinic waves, etc.

10. **Single column model**

    The SCM-WRF runs on a 3x3 stencil with periodic lateral boundary conditions in x and y. No horizontal gradients are supported in this configuration so advection is absent unless explicitly imposed. The formulation for advection in the current version is an upstream relaxation following Ghan et al. (1999).

11. 3D tropical cyclone

    Idealized tropical cyclone on an f-plane with constant SST in a specified environment. Uses capped Newtonian relaxation to mimic longwave radiation. The default setup uses the Jordan (1958) mean hurricane sounding with 28°C SST and no background winds. The analytic initial vortex is from Rotunno and Emanuel (1987). This case is useful for testing the effects of new model code (e.g., new physics options) on tropical cyclones in an idealized framework.

12. Convective-radiative equilibrium test

    Idealized 3d convective-radiative equilibrium test with constant SST and full physics at cloud-resolving 1 km grid size. Periodic b.c.s. Tropical conditions, small f and weak wind.

Also, when needed, individual users can construct other idealized configurations. In the present thesis the 1D test simulation "Single column model" is used.

2.2 Physics package and parametrisation scheme for this research

Based on a long-term research, Seibert et al. (1997) recommend using numerical boundary layer models with a good turbulence parameterization with a prognostic equation for the TKE (closure of the order 1.5) as an alternative to simple parameterisations, and they state, that one-dimensional models are fast enough to be used even for long data series. For the present simulations we use a **single column model (SCM)**. An SCM is a one-dimensional (vertical) computational model of a specific columnar region of the atmosphere (Zhang et al., 2016). An ability to run in single-column mode is a relatively new feature of WRF widely employed to evaluate boundary-layer parametrizations under well-controlled conditions. Many SCM (intercomparison) studies of the stable and unstable boundary layer have already been carried out (for example, Steeneveld et al. (2006), Cuxart et al. (2006)). The single column has a structure of a stencil of 9 grid cells (horizontal grid 3×3), the middle of which is examined. The SCM model by default has a 4 km grid size (grid spacing) and a 12 km top, has doubly periodic boundary conditions in x and y, and has the full suite of physics options available (this information is available in the description of the single column model). The SCM approach is conceptually simple and extremely quick to run (less than a minute on a laptop for a 72 h time series). Single-column models (SCMs) are powerful tools to test different parametrization schemes without the interference of the atmospheric three-dimensional (3D) dynamics (Baas et al., 2010). The model does not employ horizontal gradients or advection, but it is a good option to examine how model physics operates in a single grid column: it can be relatively straightforward to compare how different physics respond to identical forcing. The SCM has a flexible input sounding and input soil temperature/moisture file that are simple ASCII files. As we will see below, ABL schemes remain one of the primary sources of inaccuracies in model simulation. Vertical mixing is essential for the performance of ABL schemes (Hu et al., 2010). The are many ABL schemes available in the WRF model, fourteen of them are shown in Table 3 The information for Table 3 is available in the model description files (for example, namelist input). For SCM-simulations the following fundamentally different PBL parameterisations are most often used (Breuer et al., 2014): YSU – Yonsei University, MYJ – Mellor–Yamada–Janjič, QNSE – quasi-normal scale elimination, ACM2 – Asymmetric Convective Model 2, BouLac – Bougeault–Lacarrère. More information about each scheme can be found, for example, in the review of Cohen et al. (2015).

Table 3: Summary of WRF ABL parameterization schemes

key	boundary layer option	short name	closure type	ABL height definition
0	no boundary layer	-	-	-
1	Yonsei University	YSU	1.0 non-local	Ri_b calculated from sfc
2	**Mellor–Yamada–Janjič**	MYJ	1.5 local	TKE-prescribed threshold
3	Hybrid EDMF GFS scheme	-	-	-
4	Eddy-Diffusiiivity Mass Flux	-	-	Quasi-Normal Scale Elimination PBL
5	Mellor-Jamada-Nakanishi-Niino	MYNN	1.5 local	TKE-prescribed threshold
6	Mellor-Jamada-Nakanishi-Niino	MYNN 3rd level	-	-
7	Asymmetric Convective Model	ASM2	1.0 non-local	Ri_b calc. above neutral buoy. level
8	Bougeault and Lacarrere	Boulac	1.5 local	TKE-prescribed threshold
9	University of Washington	UW	1.5 local	Ri_b threshold
10	Total Energy Mass Flux	TEMF	1.5 non-local	Ri_b threshold
11	Shin-Hong “scale aware” PBL scheme	-	-	-
12	Grenier-Bretherton-McCaa scheme	GBM	1.5 closure	-
93	2015 GFS scheme	-	-	-
99	Medium Range Forecasting scheme	MRF	-	-

Basically, we can divide practically all WRF PBL models into two types, both created to simulate the turbulent PBL processes:

1. Predictive schemes. They forecast turbulent kinetic energy TKE (see, for example, equation 20) directly and use it to get eddy diffusivities as a function of height. These schemes are local-closure schemes: they do mixing between adjacent grid levels and thus may have problems in accomplishing deep PBL mixing relevant under strongly unstable conditions. Examples are the Mellor-Yamada-Janjić (MYJ) PBL scheme (Janjić (1990), Janjić (1994), Janjić (2002)) and the Mellor-Yamada-Nakanishi-Niino level 2.5 (MYNN2) PBL scheme (Nakanishi and Niino, 2009). It was shown (Mellor and Yamada, 1982), that these local closure schemes are well suited for shear turbulence in weakly stable conditions.

2. Diagnostic schemes, which rely on given PBL layer depth. Typically, they are non-local schemes.These schemes are recommended for the cases where a realistic picture of eddy structure in a convective boundary layer is needed, as in these cases the large eddies also produce turbulent mixing and local schemes are less suitable. Nonlocal schemes have an additional term to represent large-scale mixing. Examples: the Yonsei University (YSU) PBL scheme (Hong and Dudhia (2006), Hong (2010)) and the Asymmetric Convective Model version 2 (ACM2) PBL scheme (Pleim, 2007).

Each of the above mentioned PBL schemes uses its own technique to diagnose PBL heights. In the present work we are using Mellor–Yamada–Janjić scheme, which, as mentioned above, is a local closure TKE scheme of one-and-a-half order. We have chosen this scheme as we need a Coriolis-independent TKE variable (see Chapter 1 above). The governing equations are the following (Xie et al., 2012):

$$\frac{\partial e}{\partial t} = -\frac{1}{\rho}\frac{\partial}{\partial Z}\rho\overline{w'e'} - \overline{u'w'}\frac{\partial U}{\partial Z} - \overline{v'w'}\frac{\partial V}{\partial Z} + \beta\overline{w'\theta'} + D - \epsilon \tag{21}$$

$$\overline{w'u'} = -K_m\frac{\partial U}{\partial Z} \tag{22}$$

$$\overline{w'v'} = -K_m\frac{\partial V}{\partial Z} \tag{23}$$

$$\overline{w'e'} = -K_e\frac{\partial e}{\partial Z} \tag{24}$$

$$\overline{w'\theta'} = -K_h\frac{\partial \theta}{\partial Z} \tag{25}$$

In these equations e is of course the TKE, β is buoyancy coefficient, ϵ is molecular dissipation. The physics is the same as described for equation 19. Every scheme has its own formulation of PBL height, each having its limitations. In the MYJ PBL scheme: the PBL height is defined as the height of the model layer where the TKE decreases to a prescribed minimum value, 0.1 m^2/s^2 (Xie et al. (2013), Banks et al. (2016)).

There are three schemes in the SCM model responsible for physics options and that are important for our research: PBL scheme, surface layer scheme and land surface model (Tables 3, 4, 5, the information used in the tables can be found in readme files of the SCM). The surface layer scheme deals with interactions with the surface: it computes friction velocity and exchange coefficients, with which surface heat, moisture fluxes (which are then used by the land surface model if it's not

Table 4: Surface layer scheme options available in SCM model

key	option
0	no surface layer
1	Revised MM5 Monin-Obukhov scheme
2	**Monin-Obukhov (Janjič) scheme**
3	NCEP Global Forecast System scheme (NMM only)
4	QNSE surface layer
5	MYNN surface layer
7	Pleim-Xiu surface layer (ARW only)
10	TEMF surface layer (ARW only)
91	=Old MM5 scheme

Table 5: Land surface model options

key	option
0	no surface temp prediction
1	thermal diffusion scheme
2	**Unified Noah land-surface model**
3	RUC land-surface model
4	Noah-MP land-surface model
5	Community Land Model version 4 (CLM4)
7	Pleim-Xiu LSM (ARW)
8	Simplified Simple Biosphere Model (SSiB)

a water surface, otherwise the surface layer scheme computes these parameters itself) and surface stress (used further in PBL) are computed. The parameters are called `sf_sfclay_physics`. The PBL scheme uses surface layer scheme information and computes PBL height, K_m and K_h. You can define which scheme you use in the section `bl_pbl_physics` (Table 6). Finally, the land surface model (LSM) uses surface layer scheme information to compute surface fluxes of heat and moisture, interaction with soil, and effect of vegetation canopy. It is called `sf_surface_physics` in the input file.

These three schemes (PBL, surface layer scheme and LSM) are connected with each other. PBL and surface layer schemes are often paired: for example, the MYJ PBL scheme can be coupled only with the Eta-similarity surface layer scheme (Janjić, 1996). LSM can be selected independently, but not in all cases. Table 6 shows how it looks like in the file we edited for our research.

There are numerous works which have evaluated the boundary layer schemes and estimated the sensibility of the model to schemes. The most typical is to compare model simulations with different schemes with available observations (for example, lidar) or with other models. The subjects of research are so various and require so much profound previous knowledge for understanding, that it is impossible to quote or even summarise all of them. For example, Colle et al. (2015) found that WRF PBL parameterizations consistently underpredict wind speeds and predict near-surface temperature warmer than observed during the cool season and cooler during the warm

Table 6: Physics options chosen for this work, namelist input file

parameter	value
mp_physics	2
ra_lw_physics	1
ra_ws_physics	1
radt	0
sf_sfclay_physics	**2**
sf_surface_physics	**2**
bl_pbl_physics	**2**
bldt	0
cu_physics	0
cudt	0
num_soil_layers	4

season in the area of research (Cape Wind tower, New England). Banks et al. (2016) show that the WRF model tends to have a systematic cold, moist bias during daytime, most prominent at the coastal locations. These authors state that "WRF model simulations yield drastically different solutions depending on the PBL scheme used, the meteorological parameter analyzed, and the general synoptic conditions". Xie et al. (2012) compared four schemes, and the difference in results was significant for all parameters (wind speed, potential and near-surface temperature, PBL height and other). They note that local schemes produce shallow PBL heights (which could be due to larger eddies mixing through localised layers, Cohen et al., 2015) and overpredict wind speed (same as in the study of Gómez-Navarro et al., 2015). As we see, the same scheme can yield different biases dependent on the geographical location. Technical parameters like spatial resolution can also influence the results (Gómez-Navarro et al., 2015). According to Hariprasad et al. (2014), who also performed an intercomparison study of different PBL schemes in WRF model, the variations in mixing height simulation could be due to the use of different formulations for PBL height in different schemes. Thus, one can conclude that the choice of schemes and parameters for them play a significant role in the precision of results.

Figure 11 shows potential temperature versus time (x-axis) and height (y-axis) on the latitude 60°N, longitude 0° and initial wind speed u=10 m/s, calculated with Mellor–Yamada–Janjiċ and Yonsei University schemes. The calculation starts at 19.00. In the picture, MYJ scheme yields lower temperatures in June in the mornings. In December there are no diurnal cycles any more, because the ground is too cold, and the MYJ scheme begins to produce lower temperature on the second day.

The difference is even more noticeable if we calculate 30 days (Figure 12). In this time span, YSU scheme produces lower temperatures with minimum 225 K vs 244 K for MYJ scheme.

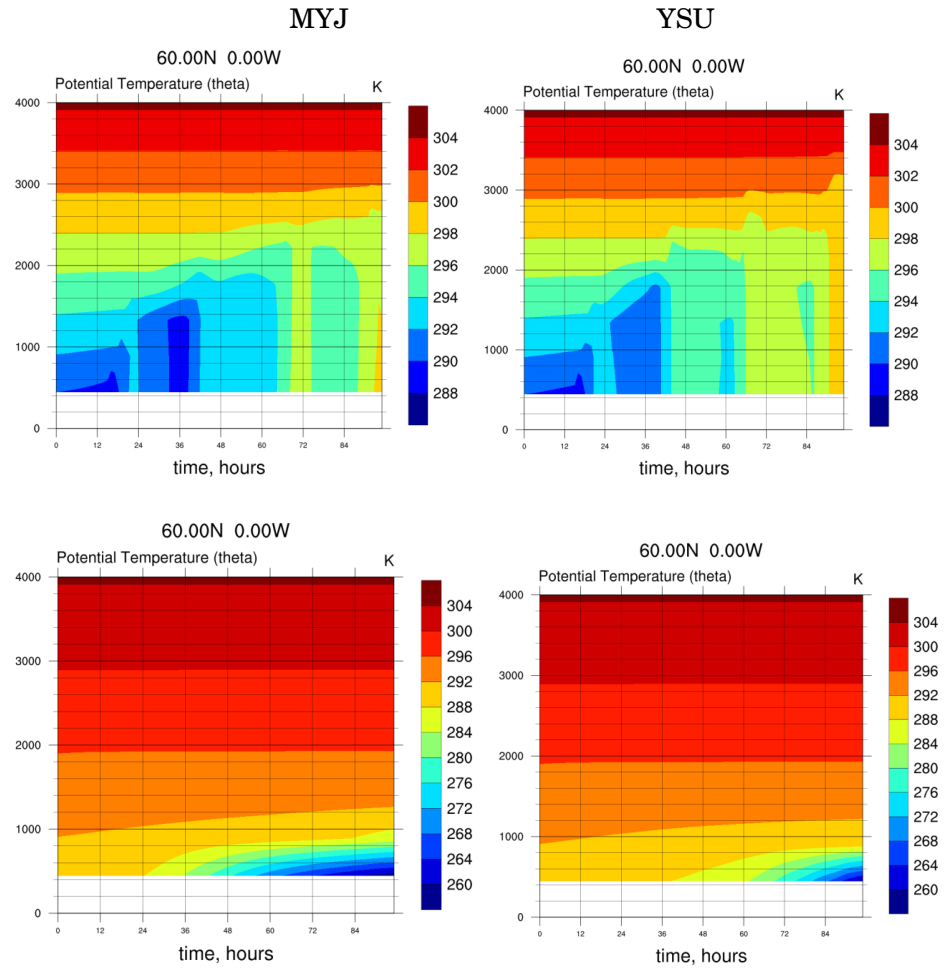

Figure 11: Potential temperature vs time and height calculated with MYJ (left) and YSU (right) schemes in June (top) and December (bottom), 3 days.

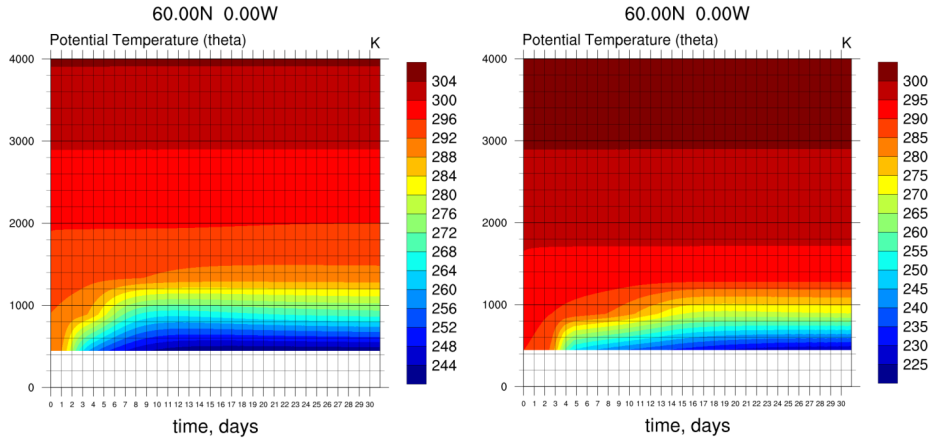

Figure 12: Potential temperature vs time and height calculated with MYJ (left) and YSU (right) schemes in December, 30 days. Note that scales are different.

2.3 Post-processing utilities

Visualisation of WRF model output data is not straightforward and requires specific post-processing tools. Basically, one can use any tool, but it is important to choose a package which, firstly, meets your objectives, and secondly, has guides and support provided. NCAR (National Center of Atmospheric Research, a US-organisation which actually developed WRF with collaborative efforts of its members and in cooperation with other organisations) supports the following tools described in WRF user's guide: NCL, Rip4, Vapor and others and others (Table 7). A growing popularity of the programming language Python is the reason why many scientists prefer this programming language for processing WRF outputs. Many documentations for WRF-Python have been created very recently, for example, a documentation by Ladwig (2018). The choice of the program depends on what you need: the program has to be able to read your data, to post-process it, if necessary, to visualise it in a way you need (2D or 3D), to have statistical functions if you need them and so on. It is also important that the program is not too difficult to use in a situation of limited time, and that it does not cost too much or is free, if you are limited in money. We have chosen the NCL, as it is the most popular programming language for WRF, it has been used for a while, is capable to read WRF-ARW data directly and can generate many types of graphical plots. Another reason is the support available for the NCL users: forum, options to ask questions ("ncl-talk").

Another programming language used in the present thesis is Python. Examples of NCL and python scripts can be found in Appendix.

Table 7: Supported post-processing packages

Package	Description
NCL	Graphical package Supported by NCAR/CISL
ARWpost	Converter (GrADS)
Rip4	Converter and interface to graphical Package, NCAR graphics
UPP	Converter (GrADS and GEMPAK)
Vapor	Converter and graphical package supported by VAPOR
IPV	GRIB (from UPP), GEMPAK, Vis5d CF compliant data (from `wrf_to_cf`). Supported by unidata
Gempark	Data from wrf2gem or UPP Supported by Unidata

3. Results

3.1 TKE and potential temperature

In this section we demonstrate some WRF simulation results with the following parameters:

- Physics options as listed in Table 6.
- 30-day runs in different seasons with initial wind speed u=10 m/s and Brunt-Väisälä frequency $N = 8.2 \cdot 10^{-3}$ s^{-1} made for different latitudes.
- non-zero heat flux (as opposed to the results of the next section).

The aim is to test the SCM model for default parameters (we change only namelist input and input sounding file without making any changes in Fortran codes) and to observe seasonal changes of TKE, potential temperature and mixing height (obtained from TKE-plots) and dependence of these parameters on latitude. For this purpose we conducted more than 200 numerical experiments for different latitudes and dates. The plots were made using NCL scripts (see Appendix for a script example) and Octave.

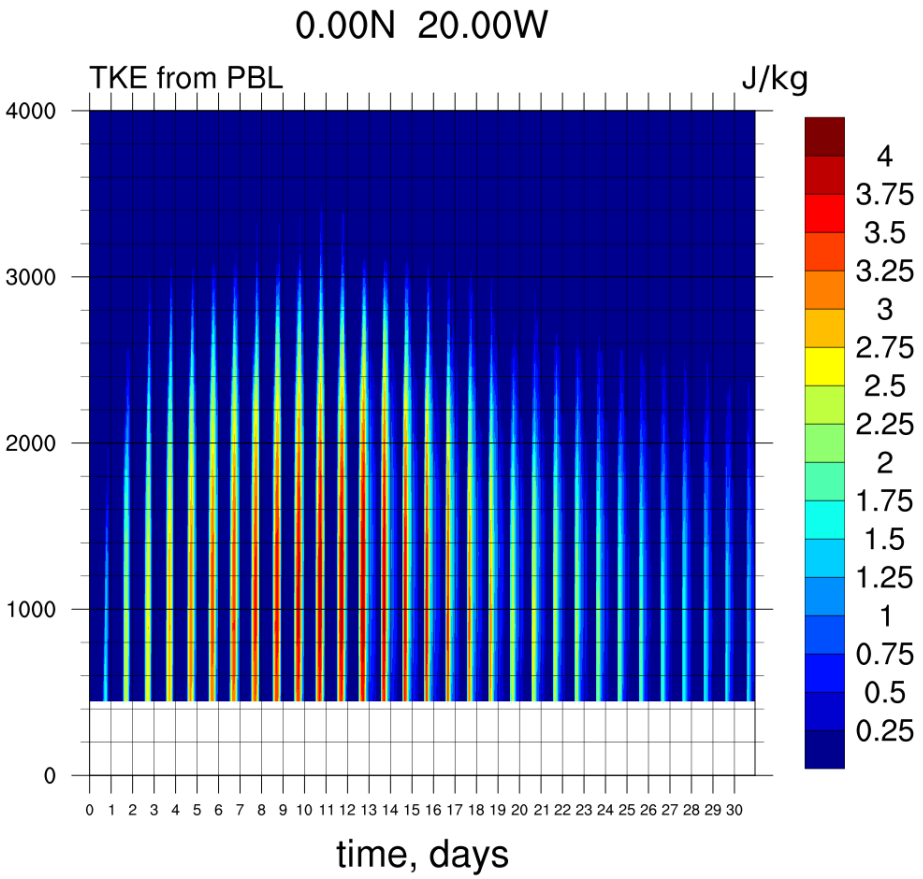

Figure 13: An example of a TKE-plot calculated with WRF and processed by NCL. Here is latitude 0°, longitude 20°, u=10 m/s, month: September.

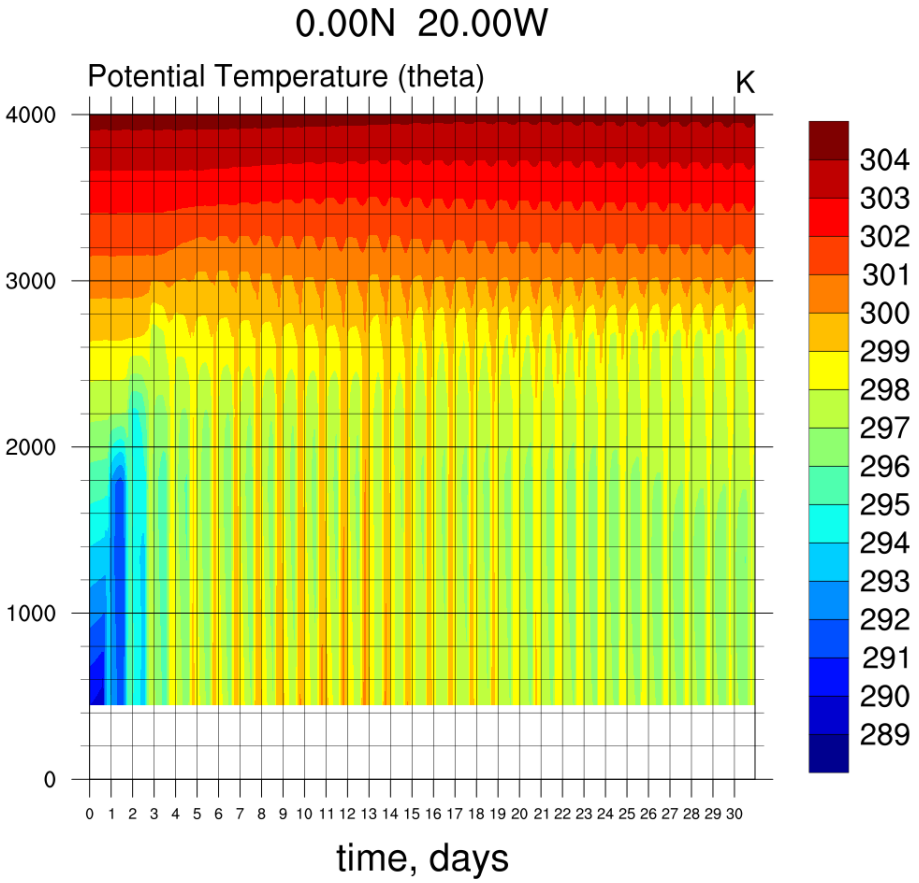

Figure 14: An example of a potential temperature plot calculated with WRF and processed by NCL. Here is latitude 0°, longitude 20°, u=10 m/s, month: September.

In Chapter 1 it was mentioned that the boundary layer height depends on the season: it is lower at night and in winter and higher at daytime and summer. Figure 13 shows TKE in a 30-day run with the simulation starting at 19.00. We can observe the diurnal cycle: the highest TKE value is in the early afternoon when the intensity of the Sun reaches its peak. As already mentioned in the Introduction (see Figure 1), one of the main sources that affects turbulence is the Sun. During the daytime, when the Sun's intensity is high, atmospheric conditions tend to be unstable and turbulence occurs. At night the intensity of solar radiation is much less than during the daytime, so the TKE values are minimum. From the scale on the right side of the plot we can read the maximum TKE value withing those 30 days: in this case it is 4 J/kg. Because mixing height is defined as the height of the model layer where the TKE decreases to a prescribed minimum value, we can assume that the values of mixing height can be read from the TKE-plots, which we do in this section. This does not yield precise values of MH, but demonstrates the correct dependencies of this parameter on latitude, date and time of the day.

Diurnal cycles of potential temperature for the same time period and the same place are shown in Figure 14. One can distinguish warmer days and cooler nights. Interesting is the time development of potential temperature in the first three days: it is obviously cooler than it could be expected in the reality.

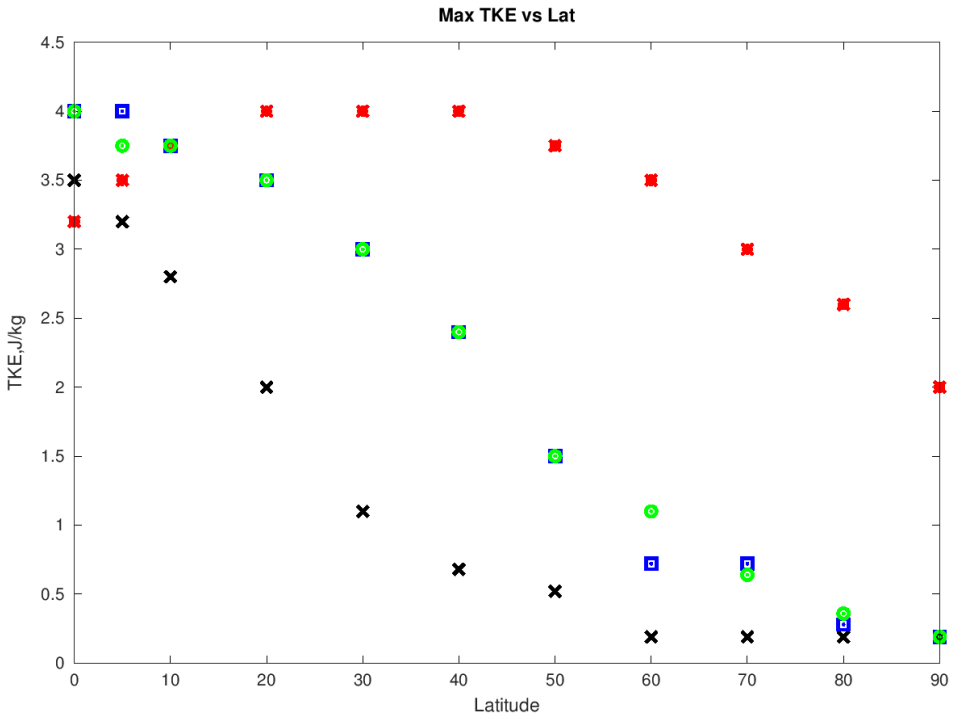

Figure 15: Maximum TKE as a function of latitude within 30 days for four seasons: winter (black crosses), summer (red stars), spring (blue squares) and autumn (green circles). Longitude: 0°, u=10 m/s.

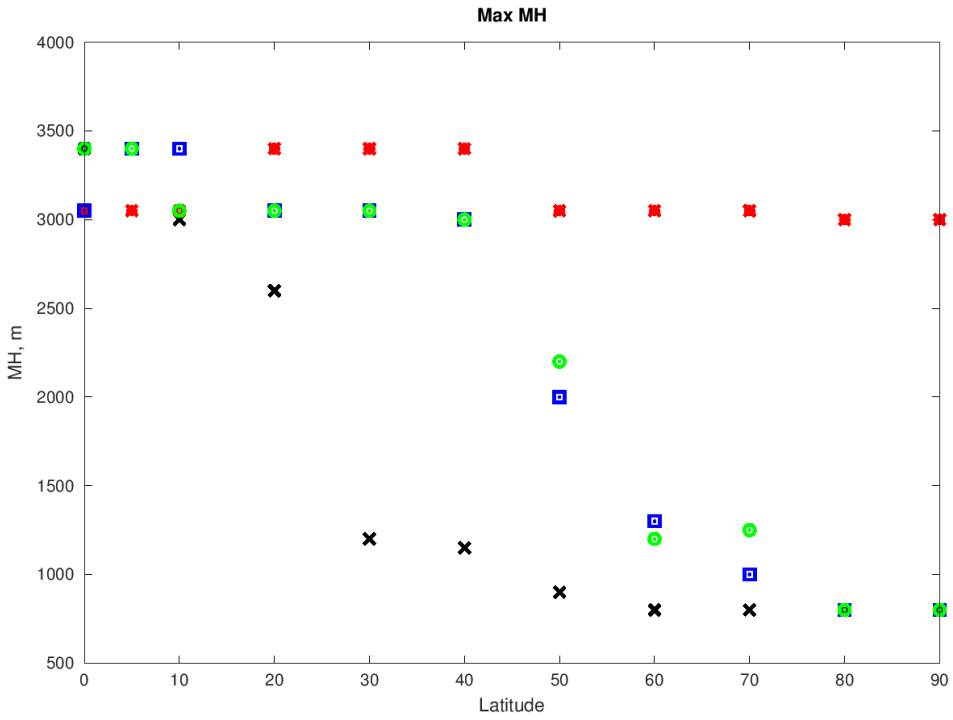

Figure 16: Maximum mixing height as a function of latitude within 30 days for four seasons: winter (black crosses), summer (red stars), spring (blue squares) and autumn (green circles). Longitude: 0°, u=10 m/s.

Figure 15 shows the dependence of maximum TKE within 30 days from the latitude. Maximum TKE and MH can be read directly from the plot (see, for example, Figure 13). The model runs for 30 days, so that the 15'th day of the simulation is the characteristic shortest day (winter), longest day (summer), or equinox days (spring and autumn). From the Figure one can conclude, that

maximum TKE decreases with latitude for winter, spring and autumn. For summer the situation is a bit different: the TKE reaches its maximum between the latitudes 20° and 40°, and after that decreases, but not so rapidly. As expected, it reaches minimum at the latitude 90°, but this value is significantly bigger than the same for winter, autumn and spring (2 vs 0.19 J/kg).

Figure 16 depicts maximum mixing height achieved in the same period of time as in the Figure 15. We see that, as it can be expected, this parameter demonstrates a good correlation with TKE in the Figure 15, having similar pattern. The only difference is the abrupt change of MH between the latitudes 40° and 60° for spring, summer and autumn and between 20° and 30° for winter compared to smooth (practically linear for spring and autumn) change of TKE.

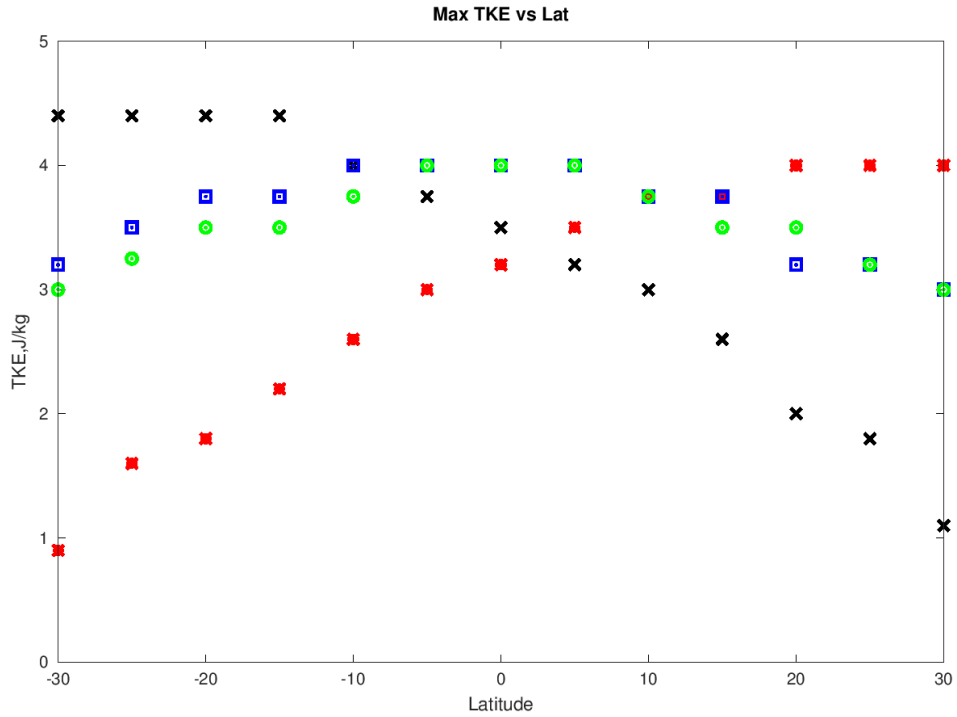

Figure 17: Maximum TKE as a function of latitude within 30 days for 4 seasons between 30°S und 30°N: December (black crosses), June (red stars), March (blue squares) and September (green circles). Longitude: 20°W, u=10 m/s.

In the Figures 17 and 18 one can find maximum TKE and MH within 30 days for four seasons for the same dates as in Figures 15 and 16 above, but for the equatorial, subequatorial and tropical areas for both hemispheres. The longitudes cover only land surface. The purpose of the figures is to demonstrate the seasonal changes and to compare the two hemispheres: the figures show assymetry for December and June (in the Figure 17 TKE continuously decreases with latitude in December and increases in June), whereas it reaches maximum on the equator for March and September. Same pattern for December and June can be found for the MH in Figure 18 , and for March and September MH changes only slightly. The reason for such behavior is simple: in summer the Earth gets more energy from the Sun, which creates more turbulence, and for the Southern Hemisphere December is a summer month.

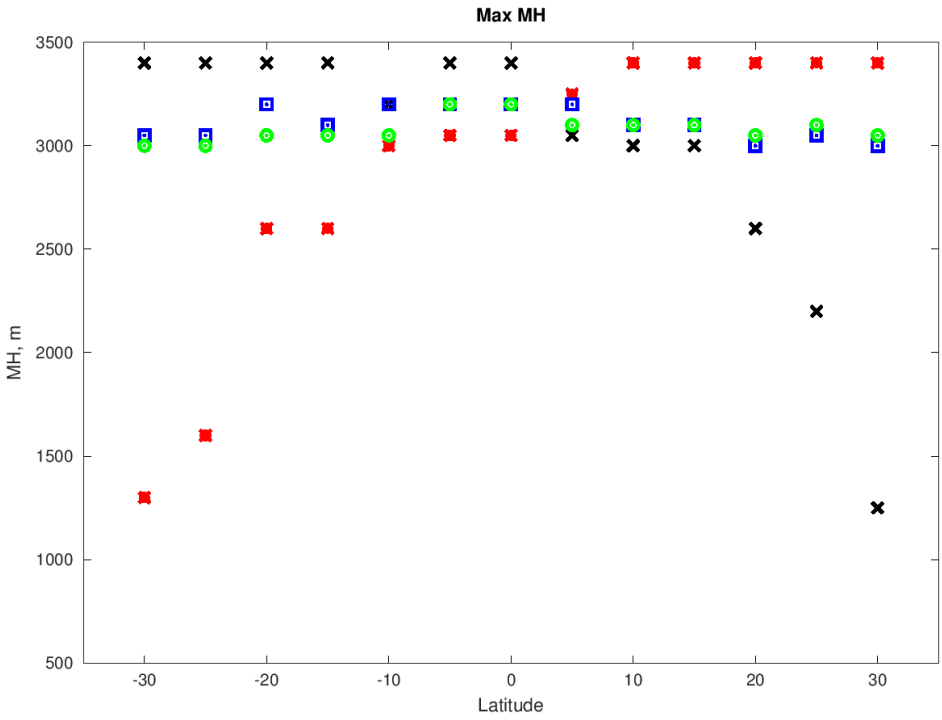

Figure 18: Maximum mixing height as a function of latitude within 30 days for four seasons between 30°S und 30°N: December (black crosses), June (red stars), March (blue squares) and September (green circles). Longitude 20°W, u=10 m/s.

.

3.2 Mixing height simulated by the idealised SCM model with zero heat flux

In this section we return to the main question of our research: the performance of simple diagnostic equations in the equatorial areas, where this parameter is zero, and the relevance of Coriolis parameter for the determination of mixing height. Here we compare the values of mixing height directly taken from the model output (we name it h_{mix}) with mixing height calculated using the equation 3 and some other popular equations (see below). In the equation 3 we use the values of friction velocity u_* yielded by the model, and a=0.2. We also study the behavior of mixing height as a function of parameters such as latitude, wind speed and stability (represented by the Brunt-Väisälä frequency) which will give us an idea about the importance and relevance of such latitude-dependent parameter as the Coriolis parameter f for the boundary layer height estimation. The stability is represented by the Brunt-Väisälä frequency (equation 6) where g is the gravity acceleration, θ is the potential temperature and z is the height above ground level.

In this section we report the results from about 200 SCM model runs with different values of latitude, initial wind speed and Brunt-Väisälä frequency. For obtaining the values of h_{mix} and u_* from the model, after every run we make a log-file with certain print statements. Then a python script (See Appendix 2) reads this file, extracts the variables h_{mix} and u_* together with the time information, calculates the value of h with the equation 3, calculates average values for the whole time period and prepares all these values for plotting by creating a text file with a matrix of values. These values can be then plotted with any application program (here Grace and Excel are used).

As opposed to the cases described in the previous section, here we set surface heat flux to zero in order to get a neutral boundary layer with no evaporation. We initialize the atmosphere with neutral stratification (e.g. Table 8). For this purpose we have made the following changes in the source code of the subroutine `phys/module_sf_scmflux.F` located in the physics package of the model:

line 121:

Original:
```
hfx_force = hfx_force + dt*hfx_force_tend
```
New version:
```
hfx_force_tend = 0.
```

line 99-100:

Original:

```
hfx_interp=fc_hfx(n)+(fc_hfx(n+1)-fc_hfx(n))*

*(julian_in-fc_julian(n))/(fc_int/86400.)
```

New Version:
```
hfx_interp = 0.
```

line 141:

Original:
```
hfx(i,j)=amax1(hfx(i,j),-250.)
```

New version:
```
hfx(i,j) = 0.
```

After the model is compiled, the heat flux is zero.

Table 8 shows one of the variants of the input sounding file, which we use for these simulations. In the table, z is the height $z_{terrain}$ above the ground in m, u and v are initial wind speed at the height of 10 m, the column θ defines the potential temperature profile (in K), and q_s is water vapour in kg/m^3. To simplify the conditions, we set the y-component of initial wind speed zero, as well as the moisture above the ground. The latter has to be set 0, because we eliminate the heat flux. In process of work we change the temperature profile (Brunt-Väisälä frequency) and initial wind speed u, in order to obtain the dependences in Figures below. The duration of runs is 60 days.

Table 8: A sample input sounding file.

z	u	v	θ	q_v
0.0	10.0	0.0	290	0.0025
1000.0	10.0	0.0	292	0.0
2000.0	10.0	0.0	294	0.0
3000.0	10.0	0.0	296	0.0
4000.0	10.0	0.0	298	0.0
6000.0	10.0	0.0	302	0.0
8000.0	10.0	0.0	304	0.0
9000.0	10.0	0.0	316	0.0
10000.0	10.0	0.0	328	0.0

The parameters stated in the Table 8, as well as the absence of heat flux, define an unrealistic and very simplified situation. In this case the one real mechanism that is influencing the atmosphere is turbulence. Figures 19 show potential temperature θ and TKE as a function of time and height, same as Figure 13, but in 60 days: in the situation of zero surface heat flux we do not observe any diurnal cycles at all. Season and longitude are also unimportant for such simulations, which makes it easier to estimate the relevance of the Coriolis parameter f, the latter being a function of latitude only. One can notice that there is no turbulence at the equator (top left): the TKE is very low. We performed model runs for equator for different values of wind speed, but the situation remained the same: no turbulence.

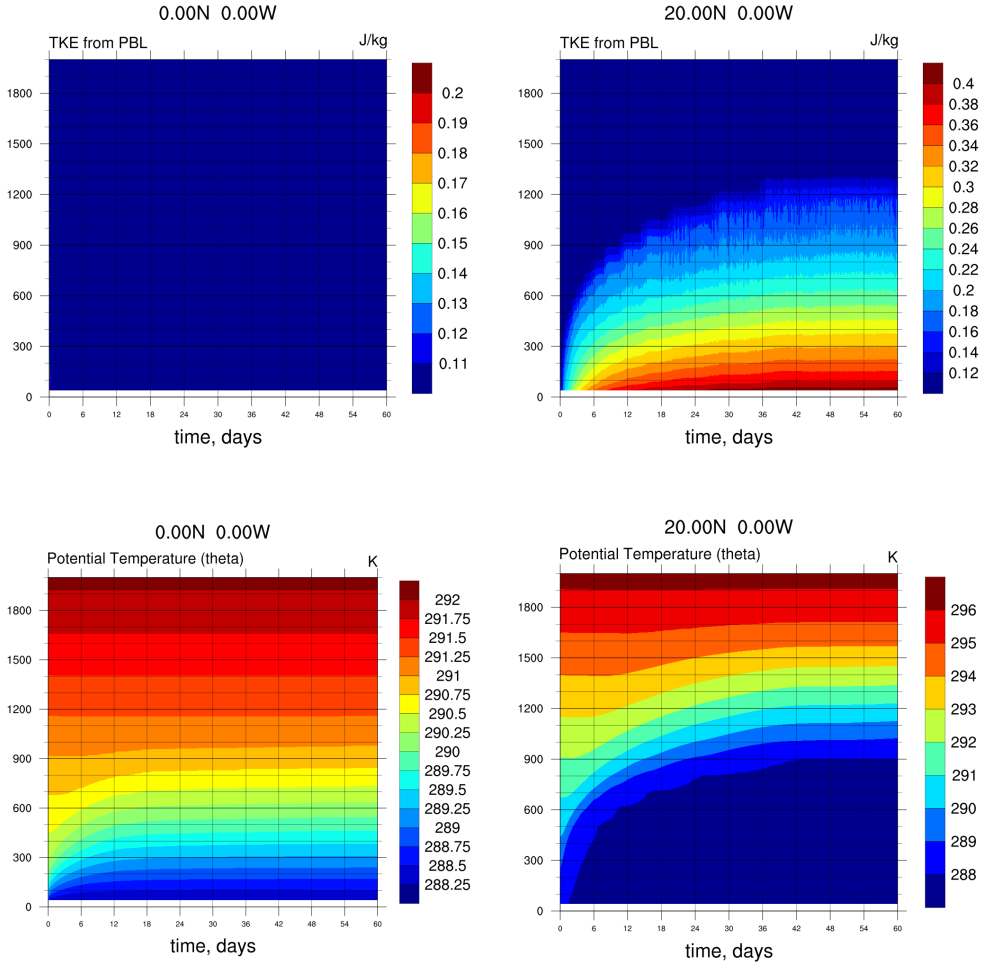

Figure 19: TKE (top) and potential temperature (bottom) as a function of time and height for ϕ=0 (left) and ϕ=20° (right). Initial wind speed u=10 m/s. Note: different scales in the figures!

Figure 20 shows the behaviour of mixing height calculated by model (black) and as a function of time in 60 days. One cannot avoid paying attention to two interesting facts:

1. the mixing height grows rapidly within first few days, reaching the half of its value in less than two days, and after the tenth day it changes insignificantly and reaches saturation.

2. Mixing height oscillates before it settles at a new, higher value. Red line in this figure shows mixing height calculated with equation 3, which has obviously much higher values.

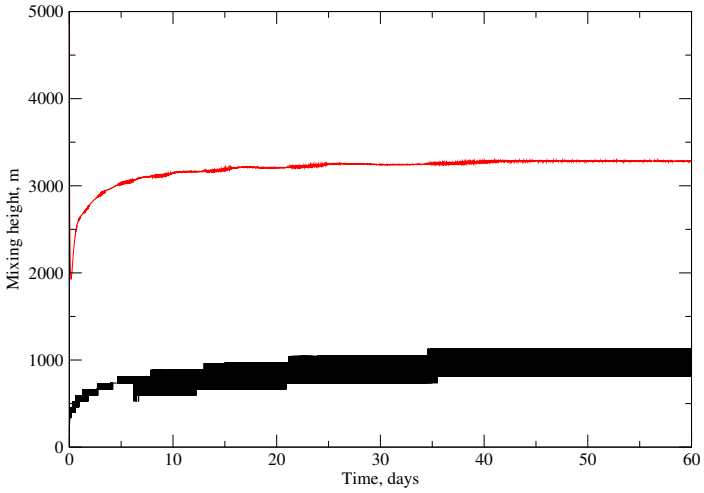

Figure 20: The time series of mixing height calculated by model (black) and from Eq. 3 using u_* (red). Initial wind speed u=10 m/s; ϕ=50°.

Figure 21 shows mixing heights h_{mix} (model output, top) and h (calculated with equation 3 using u_* from the model, bottom) as a function of latitude for 3 initial wind speeds u: 5 m/s, 10 m/s and 20 m/s. Here, as well as in Figure 25 and 27, $N = N_1 = 5.81 \cdot 10^{-3}$ s^{-1}. In the Figure, mixing height h_{mix} grows with latitude between 1° and 15° and then reaches saturation for the initial wind speed u = 5 m/s. For higher wind speeds it first grows in low latitudes and reaches maximum between 1 and 10°, and then decreases to some value which remains constant in higher latitudes. The function $h(\phi)$ (calculated with equation 3 using u_* from the model) has the same pattern for all wind speeds: it rapidly decreases with increasing latitude in equatorial and tropical regions, then slowly decreases in midlatitudes and stays practically the same in polar regions. The functions $h_{mix}(\phi)$ and $h(\phi)$ have similar behaviour for higher latitudes (50° and higher): mixing height stays almost constant. But for lower latitudes the trends are completely different (see Figures).

This is especially obvious in Figure 22, which compares the mixing height calculated by model and equation with each other, and for that purpose due to the big differents in height values a plot in the log-scale has been made.

The ratio of mixing height to friction velocity h/u_* grows with $1/f$ (which means it declines with the Coriolis parameter and with latitude), however it is not directly proportional to $1/f$ (Figure 23).

In Chapter 1, in the Section "Methods of research of boundary layer" Table 1 with eight different diagnostic equations was mentioned. Figure 24 shows mixing height as a function of latitude for wind speed u=10 m/s as a result of calculation of the WRF model, equation 3, an equation by Steeneveld et al. (2006) ($h = 10u_*/N$, as derived from equation 7) and four equations from this Table. The value u_* is taken directly from the model. In equations suggested by Arya (1981) and Mahrt et al. (1982), as well as equation 3, mixing height is indirectly proportional to the Coriolis parameter. This is why these equations cannot be used for equatorial and tropical regions. Here we can also notice, that the equations of Arya (1981) and Mahrt et al. (1982) show less discrepancy with the values yielded by model than equation 3. In the equations by Benkley and Schulman (1979) and Nieuwstadt (1984) mixing height is directly proportional to wind speed u. The plot

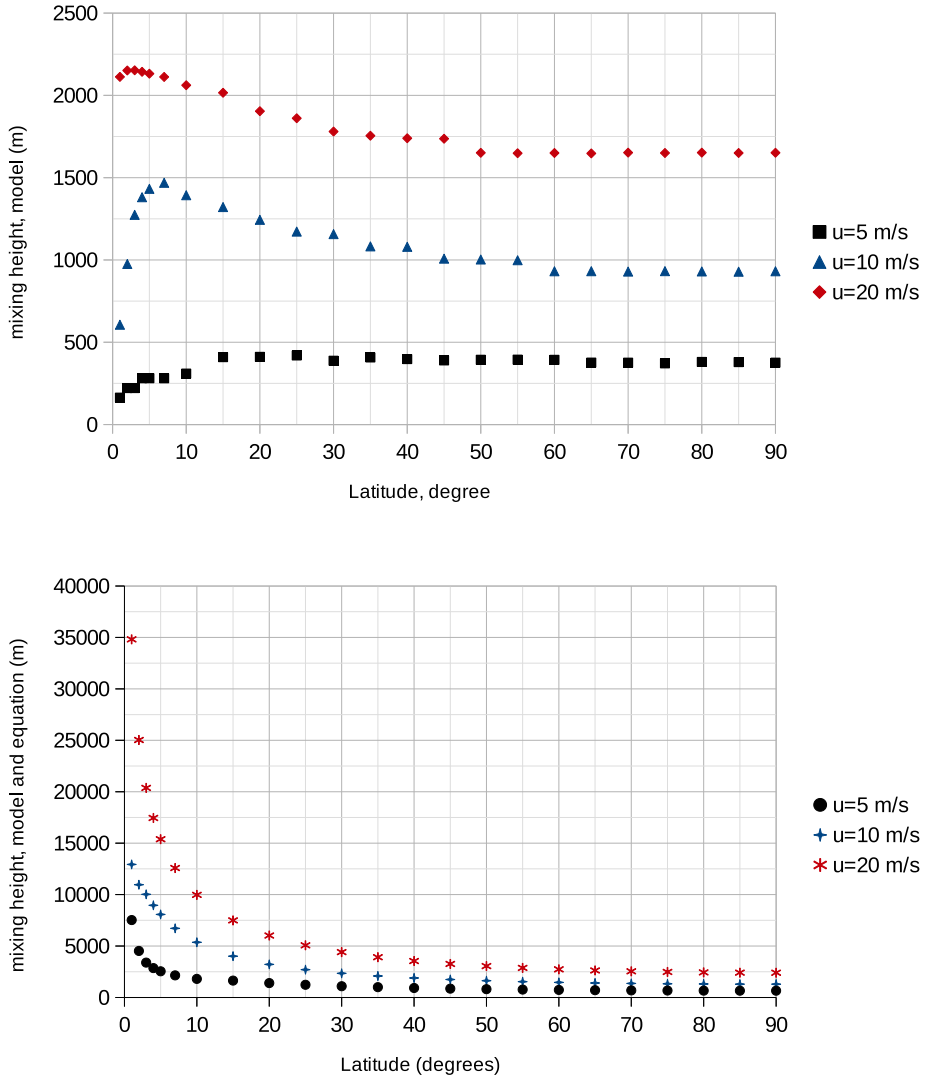

Figure 21: Mixing height as a function of latitude for three wind speeds (legend): calculated by model (top) and from Eq. 3 using u_* from the model output (bottom).

shows that the best agreement with the model is provided by Steeneveld et al. (2006): even though it underestimates model values, is has a similar trend: the height grows in the equator area and then reaches saturation and remains practically constant for higher latitudes. The reason for this behaviour is simple: the mixing height in Steeneveld et al. (2006) is proportional to friction velocity u_*, the latter is a) taken from the model b) is a measure of turbulence as itself.

The dependence of mixing height on friction velocity looks very similar to the one on initial wind speed u (Figure 26).

Figure 27 depicts the modeled and calculated mixing height for ϕ in range 1 to 90° and for three values of initial wind speed. It is clear that the equation 3, as expected, extremely overestimates the mixing height in lower latitudes, which makes it impossible to use it for such estimations. It happens due to the Coriolis parameter f. But the discrepancy is obvious also for midlatitudes, as equation 3 overestimates the values.

Figures 28 and 29 show the dependence of h_{mix} and h on initial wind speed for two latitudes for 3 values of N: $N_1 = 5.81 \cdot 10^{-3}$, $N_2 = 8.2 \cdot 10^{-3}$ and $N_3 = 1.2 \cdot 10^{-2}$ s^{-1}. The difference between the

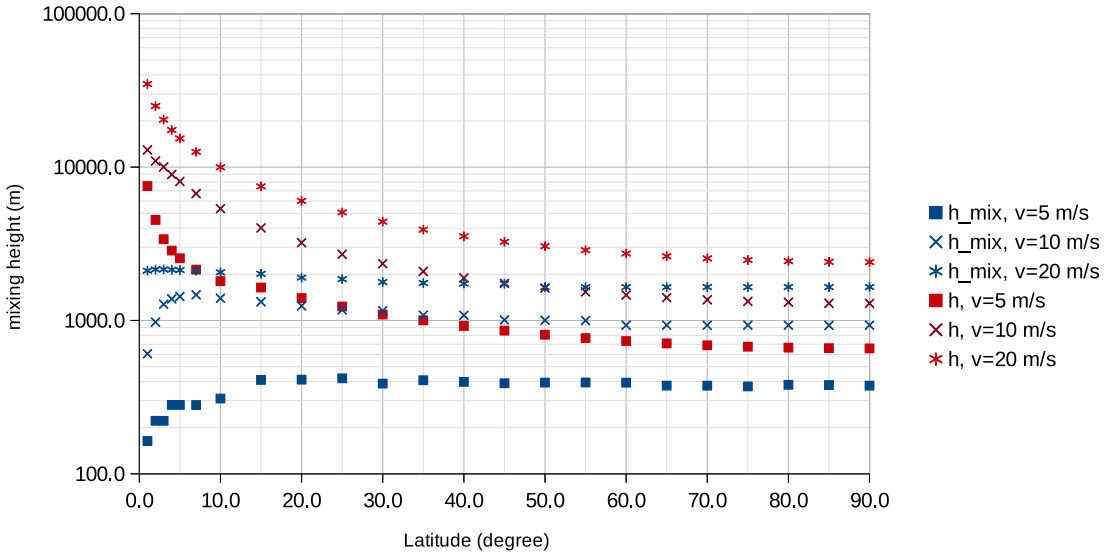

Figure 22: Mixing height: model (blue) and from Eq. 3 using u_* (red) for three wind speeds. Logarithmic scale.

.

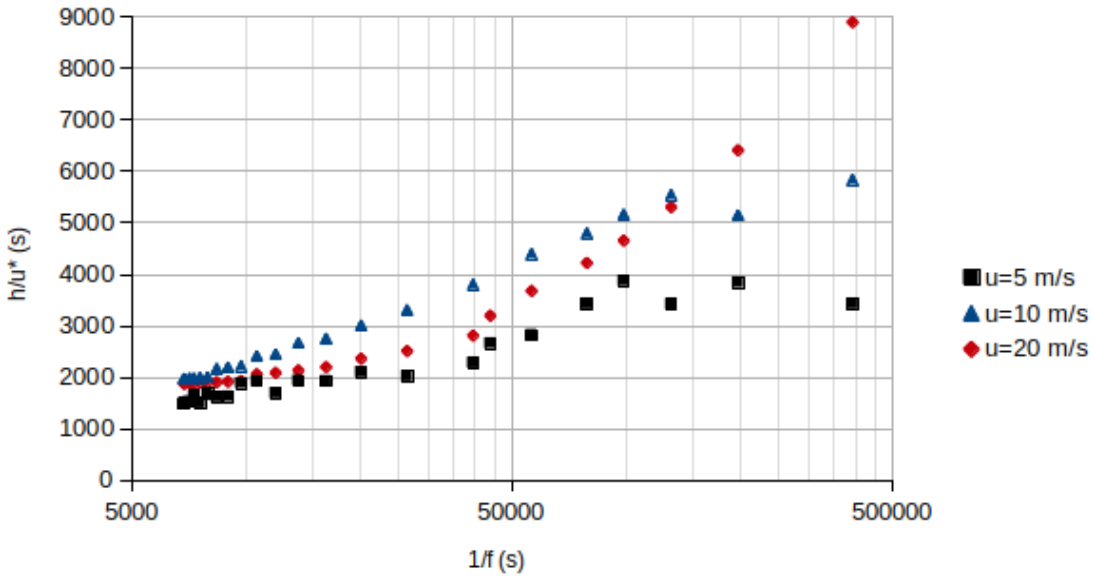

Figure 23: Ratio of mixing height h_{mix} calculated by model to friction velocity u_* as a function of $1/f$ for three wind speeds. Logarithmic x-axis.

values of h_{mix} for different stabilities is more noticeable for the lower latitude $\phi = 20$ than for $\phi = 50$: lower stability yields higher values of mixing height, which could be expected. For h value of the Brunt-Väisälä frequency does not play any role: (Figure 29, bottom).

In Figure 30 the dependence of mixing height (calculated by WRF model) on Brunt Väisälä frequency is shown. The mixing height is obviously lower for higher stability (which could also be expected). N has a stronger influnce on the mixing height for lower latitudes which can make us suggest that it is an important parameter on the equator.

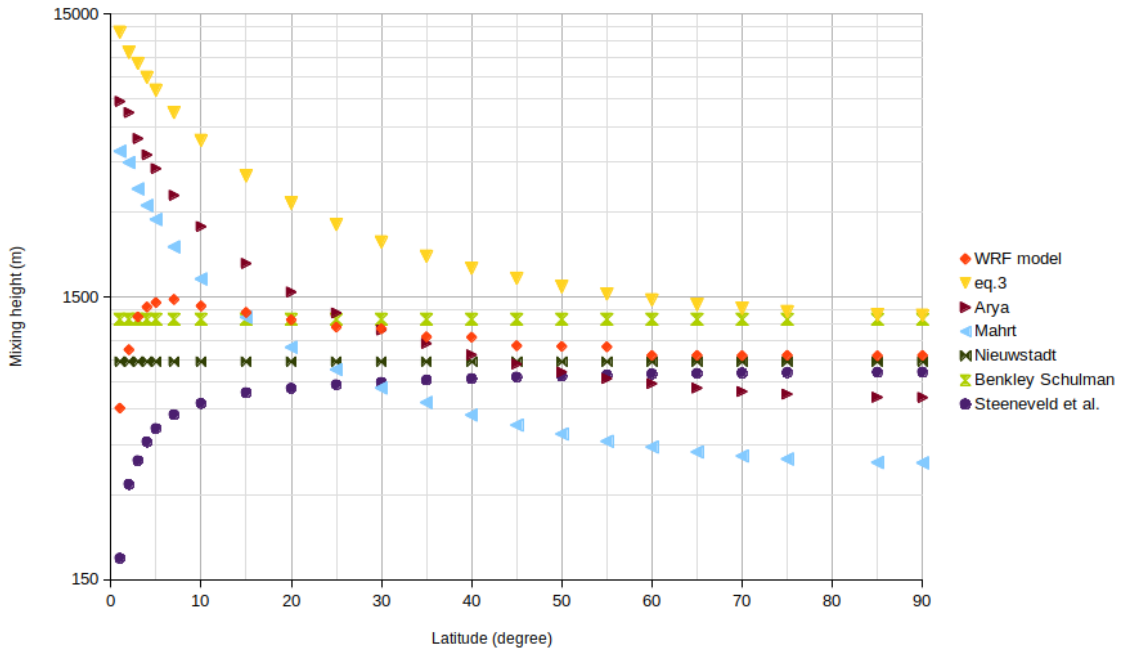

Figure 24: Mixing height as a function of latitude derived from model simulations and from different diagnostic equations (legend). Y-axis has a logarithmic scale.

Table 9: Initial potential temperature profile for cases depicted in Figure 32.

height, m	θ
0	290
1000	291
2000	292
3000	293
4000	294
6000	296
8000	300
9000	312
10000	324

Concerning Brunt-Väisälä frequency, a diagnostic equation by Steeneveld et al. (2006) under certain conditions (the stratification should be near neutral) contains N: $h = 10u_*/N$. Figure 31 shows mixing height versus friction velocity, WRF model and this equation for two values of N, and friction velocity is taken from the model. In both cases the equation underestimates the model value of mixing height, but for stabler conditions the discrepancy is much higher.

Figure 32 depicts mixing height versus initial wind speed as a result of model simulation for N=0.00581 s^{-1} (the initial profile of θ is shown in Table 9), ϕ=20°, and calculated using the equations from the Table 1 and equation 3. In the Figure, the best agreement with the model is shown by the equation of Mahrt et al. (1982), which contains the Coriolis parameter, but is also directly proportional to friction velocity u_*. That could mean that, though a general equation may still be impossible to define, simple diagnostic equations can yield a satisfactory prediction of mixing height in certain conditions.

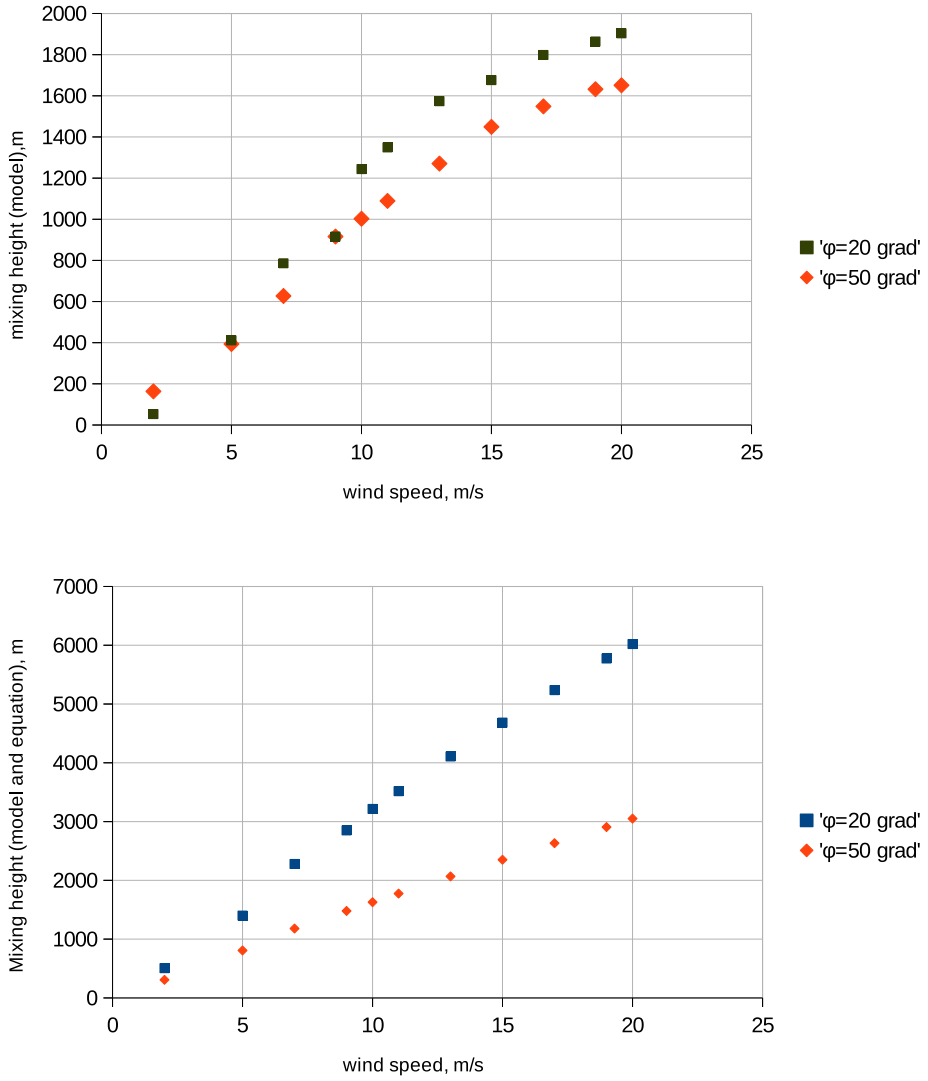

Figure 25: Mixing height as a function of initial wind speed for two latitudes (legend): calculated by model (top) and from Eq. 3 using u_* (bottom).

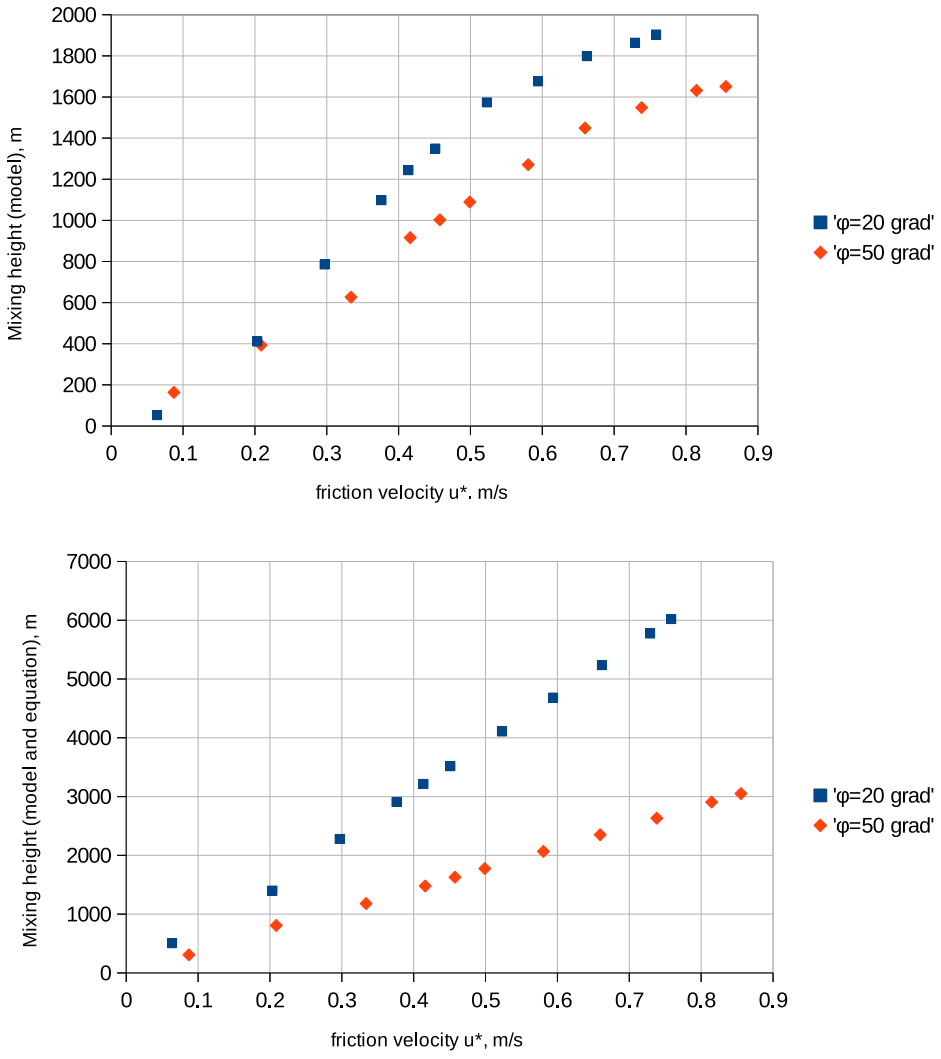

Figure 26: Mixing height as a function of friction velocity $u*$ for two latitudes (legend): calculated by model (top) and from Eq. 3 using u_* (bottom).

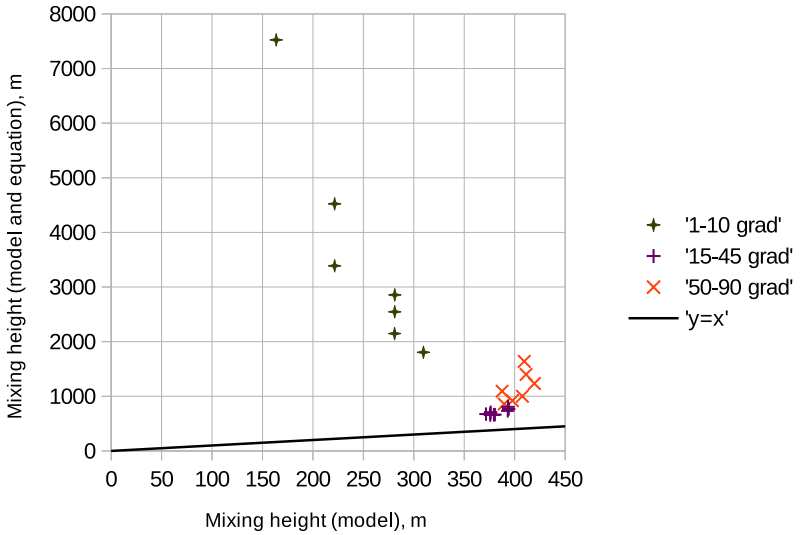

[u=5 m/s]

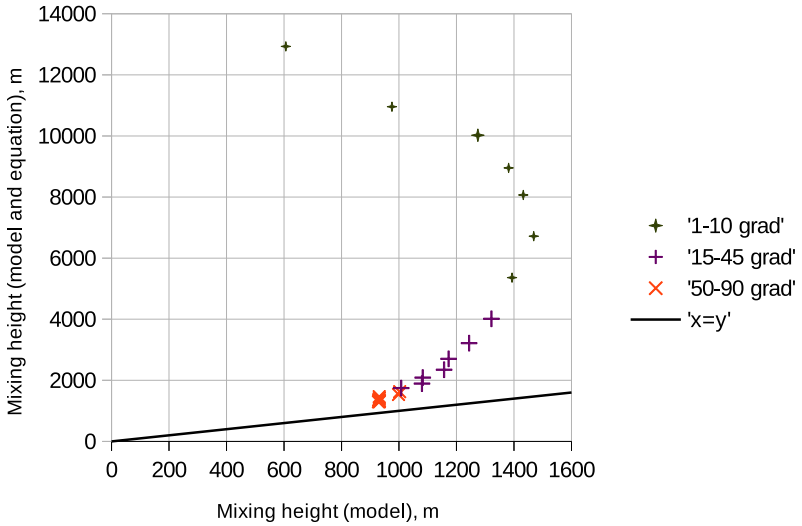

[u=10 m/s]

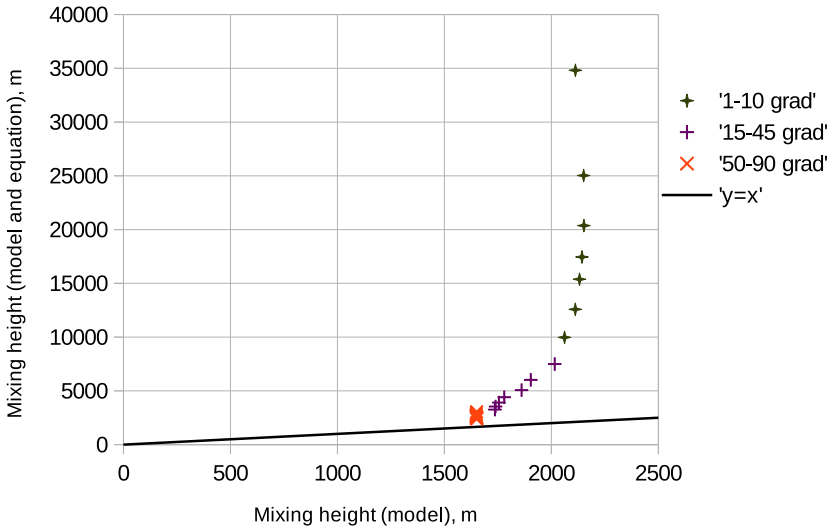

[u=20 m/s]

Figure 27: Mixing height (model output) versus mixing height calculated with equation 3 using u_* for three initial wind speeds. Solid line shows function y=x.

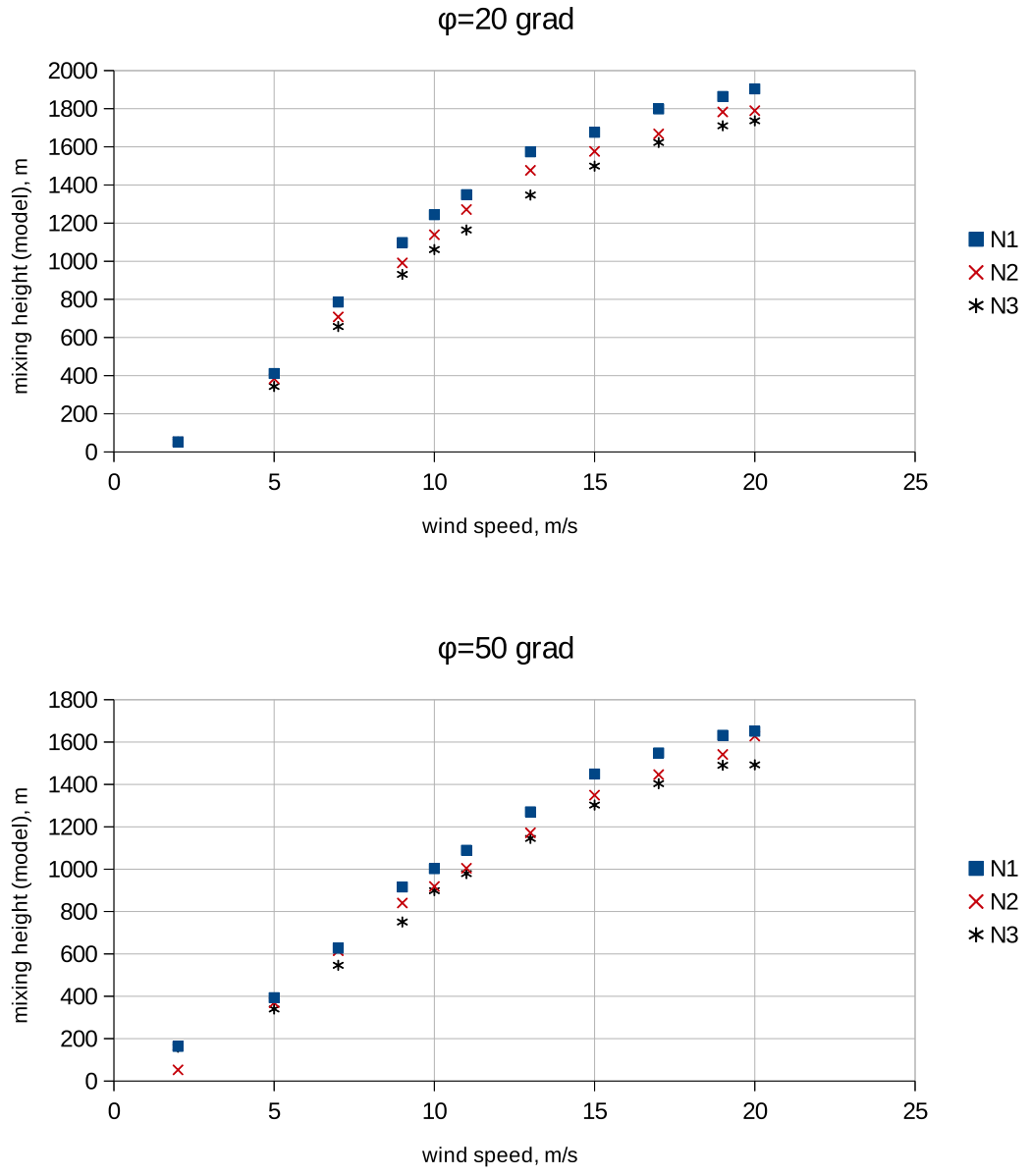

Figure 28: Mixing height calculated by model as a function of initial wind speed for three values of the Brunt-Väisälä frequency $N_1 = 5.81{\cdot}10^{-3}$, $N_2 = 8.2{\cdot}10^{-3}$ and $N_3 = 1.2{\cdot}10^{-2}$ s^{-1} for two latitudes: ϕ=20° (top) and ϕ=50° (bottom).

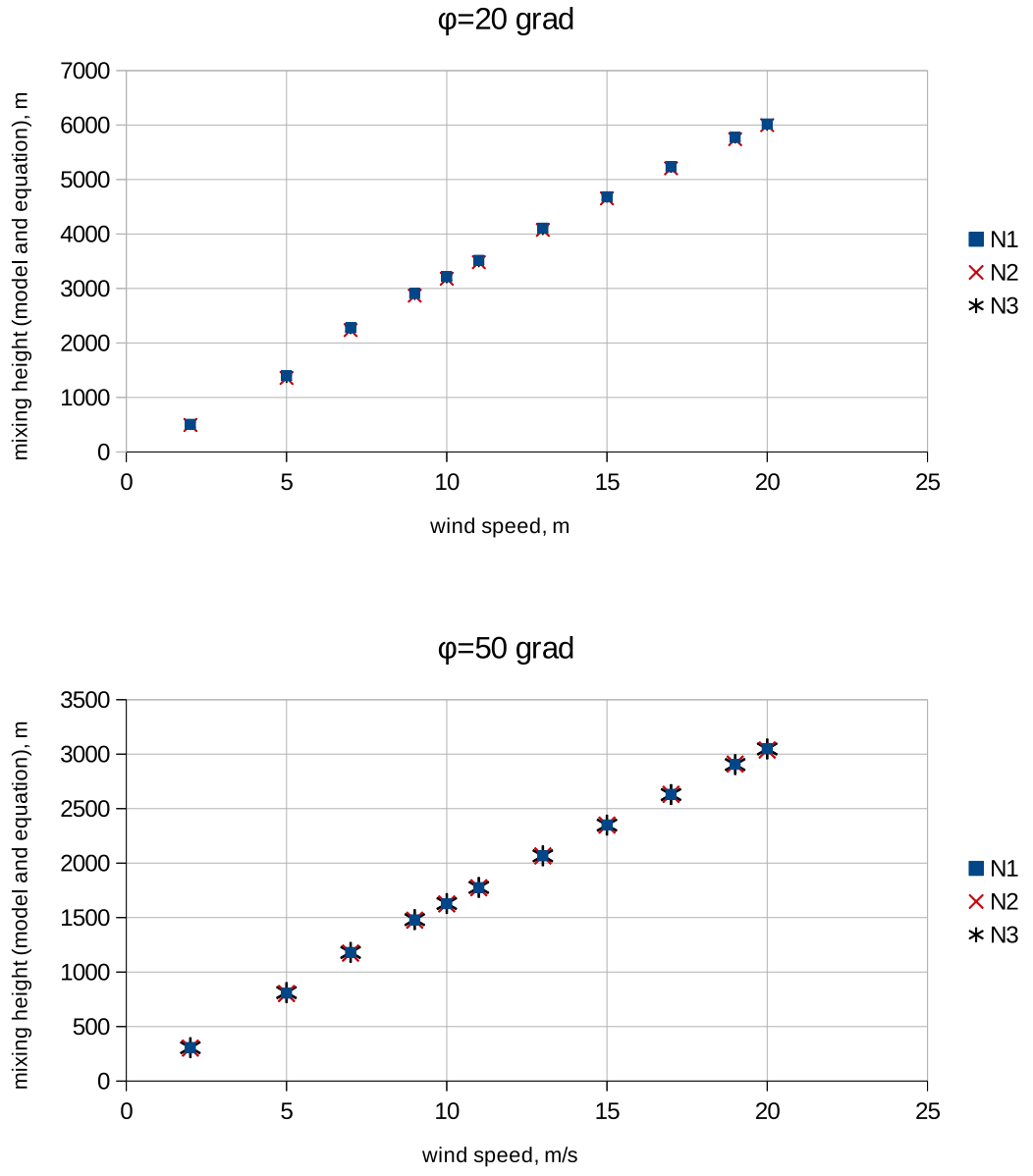

Figure 29: Mixing height calculated with equation 3 using u_* from model output as a function of initial wind speed for three values of the Brunt-Väisälä frequency $N_1 = 5.81{\cdot}10^{-3}$, $N_2 = 8.2{\cdot}10^{-3}$ and $N_3 = 1.2{\cdot}10^{-2}$ s^{-1} for two latitudes: ϕ=20° (top) and ϕ=50 ° (bottom).

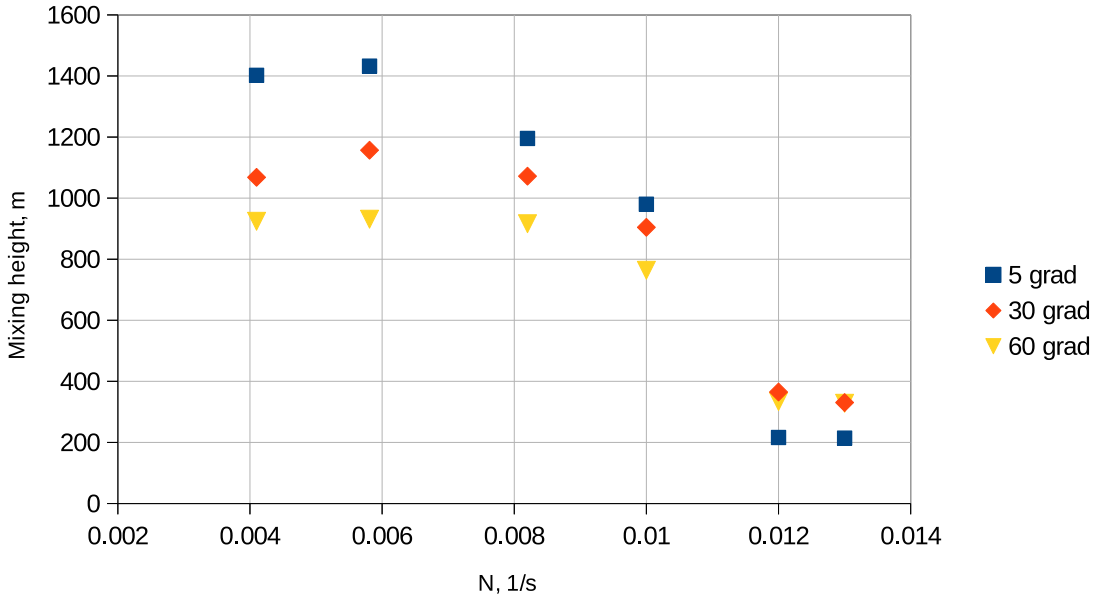

Figure 30: Mixing height as a function of Brunt Väisälä frequency for three latitudes. Initial wind speed u=10 m/s.

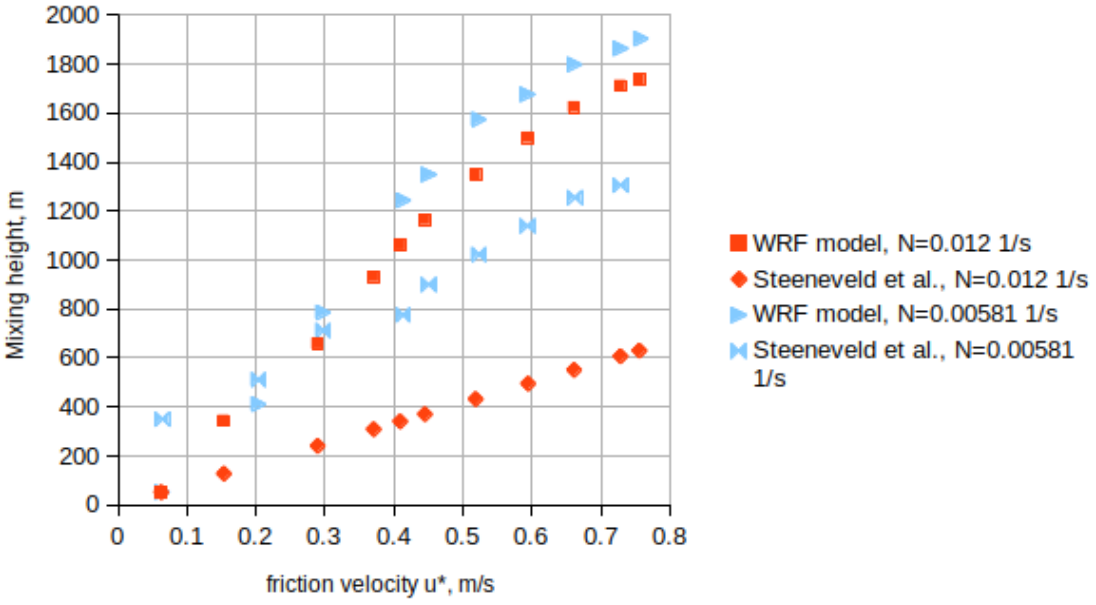

Figure 31: Mixing height as a function of friction velocity for ϕ=20° and two values of N (legend).

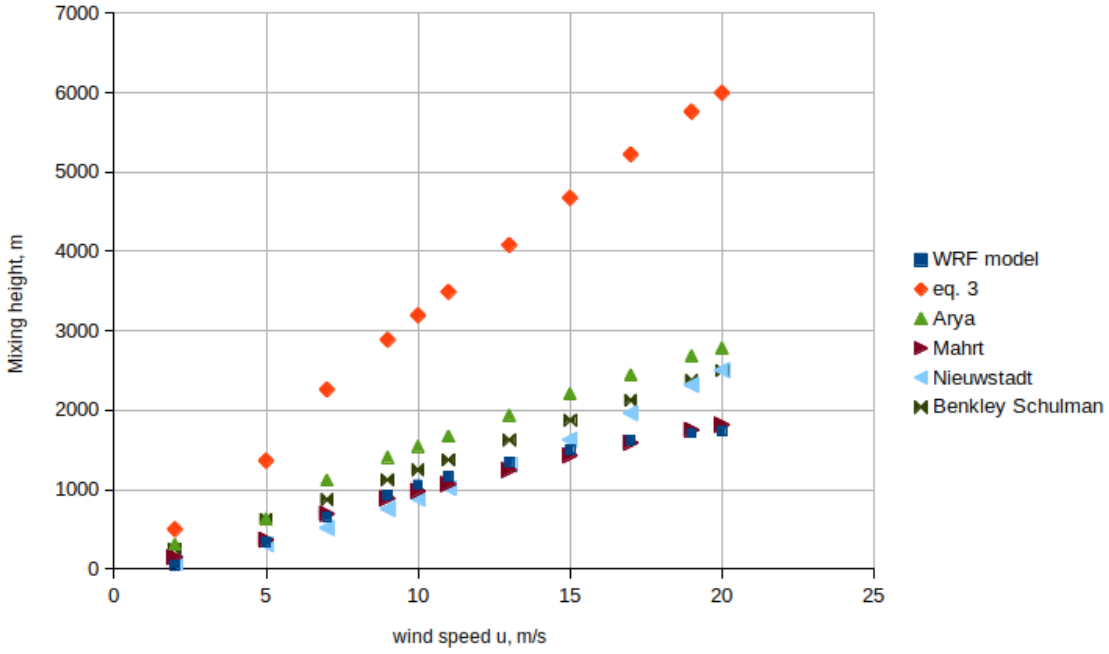

Figure 32: Mixing height versus initial wind speed calculated by model and via different diagnostic equations (legend). N=0.00581 s^{-1}, ϕ=20°.

3.3 Conclusion

On the base of the results discussed in the previous section we can draw the following conclusions:

1. The literature review which we conducted for this study shows that there is still a lack of research of mixing height in the equator area, and most of the work done in this direction is observational research.

2. The Coriolis parameter f is a function of latitude ϕ. If mixing height were indeed proportional to f^{-1}, it would be steadily decreasing with latitude. However, the results of the SCM simulations described in Section 3.2 show that already for the latitude 50° and higher the mixing height remains constant (Figures 21, 22, 24).

3. There is an explicit dependence of mixing height on initial wind speed u or friction velocity u_* respectively (Figures 25, 26, 28) which agrees with results of Steeneveld et al. (2006). The dependence on N is also significant and is more visible for the lower latitudes (Figure 30).

4. Mixing height is not indirectly proportional to the Coriolis parameter (Figures 21, 23), as certain widely-used analytical formulae assume.

5. Many popular diagnostic equations, with or without the Coriolis parameter, are not capable of yielding realistic results near equator (Figures 22, 24, 27, 31). Simple diagnostic equations cannot be used universally (Figures 24, 32).

6. In the absence of surface heat flux, the SCM model is unable to calculate a mixing height exactly on equator (ϕ=0). This could be a problem of the numerical formulation. Further research is needed to answer the question why mixing height decreases towards equator.

7. The simplified simulations with WRF model and simple diagnostic equations predict the same behaviour of mixing height as a function of latitude in higher latitudes: it stays almost constant. (Figure 24).

A. NCL and Python scripts

A.1 NCL Script: potential temperature vs time and height

```
load "/home/alina/Diplom/WRFV3/ncl64/lib/ncarg/nclscripts/csm/gsn_code.ncl"
load "/home/alina/Diplom/WRFV3/ncl64/lib/ncarg/nclscripts/csm/gsn_csm.ncl"
load "/home/alina/Diplom/WRFV3/ncl64/lib/ncarg/nclscripts/wrf/WRF_contributed.ncl"
load "$NCARG_ROOT/lib/ncarg/nclscripts/contrib/cd_string.ncl"

begin
;---Open file; substitute your own WRF output file here
f = addfile ("/home/alina/Diplom/WRFV3/test/em_scm_xy/wrfout_d01_2018-06-09_19:00:00.nc","r")

; Read character variable Times
; Convert to units of "hours since" for plotting purposes
;
times = f->Times
Time   = wrf_times_c(f->Times, 0)  ; convert to "hours since"
print(Time)

time = -1        ; -1 means all time steps

tc0 = wrf_user_getvar(f,"theta",time)   ; potential temerature

z  = wrf_user_getvar(f,"z",time)    ; z on mass points

; Vertically interpolate to height coordinates ("z")
height = fspan(0,2000,10)
tc_full = wrf_user_intrp3d(tc0,z,"h",height,0.,False)
printVarSummary(tc_full)

nlat = 1
nlon = 1
tc   = tc_full(:,:,nlat,nlon)             ; W(Time,bottom_top_stag)

printVarSummary(tc)
tc&Time := Time
printVarSummary(tc)
print(tc&Time)

;---Use simple array syntax [like f90] to change units

tc@units   = "K"

printVarSummary(tc)
```

```
;---Add/change meta data to conform to netCDF convention standards
tc!0       = "Time"
tc&Time    =  Time
tc!1       = "z"                      ; name dimensions
tc&z       =  height                       ; assign values to named dimensions

printVarSummary(tc)

;---For plot purposes only, read the specific lat/lon point
lat       = f->XLAT(0,nlat,nlon)
lon       = f->XLONG(0,nlat,nlon)
;
; create plots
; (1) A "BlWhRe" is often selected tchen plus/minus are of interest
; (2) The "symMinMaxPlt" procedure determines contour limits
;     that are symmetric.
; (3) Use the "sprintf" function to format the title
; (4) Because the rightmost dimension tcill become the "x" axis
;     use NCL's "dimension reordering" to reshape
;
wks = gsn_open_wks("png","PotTemp")

res                       = True            ; plot mods desired
res@gsnMaximize           = True            ; maximize plot size
res@cnFillOn              = True            ; turn on color
res@cnFillPalette         = "matlab_jet"        ; set the color map
res@cnLinesOn             = False           ; turn off contour lines
res@lbOrientation         = "vertical"      ; vertical label bar
res@trYReverse            = False            ; reverse y axis
res@tiXAxisString         = Time@units      ; label bottom axis tcith units attribute
res@tmXMajorGrid        =  True                   ;-- turn on grid lines
res@tmYMinorGrid        =  True
res@tmYMajorGrid      =  True
res@tmXMajorGridThicknessF=1

res@tmXBMode = "Explicit"
res@tmXBValues = ispan(0,96,12) ;
res@tmXBLabels = (/"0","12","24","36","48","60","72","84","96"/)
res@tmXBLabelFontHeightF = 0.01
res@tiXAxisString   = "time, hours"

res@tiMainString          = sprintf("%4.2f", lat)+"N  " \
+ sprintf("%4.2f", fabs(lon))+"W"

printVarSummary(tc)
plot                      = gsn_csm_contour(wks,tc(z|:,Time|:),res)
```

```
end
```

A.2 Python script: mixing height, friction velocity and other variables

```
-*- coding: utf-8 -*-
"""
Created on Fri Feb  8 12:52:09 2019

Read a wrf log file containing certain print statements.
Extract them together with time information and prepare for plotting
@author: Petra Seibert
"""

import sys
import datetime as dt
import math

fn = sys.argv[1]

if fn[:7] != 'log.wrf':
exit('stop \n log file name must begin with "log.wrf"!\n')

fnout = 'ablhgt_'+fn[7:]+'.dat'
rlat = float( fn[7:].split('_')[1] )
V = float( fn[7:].split('_')[2].split('.')[0] )
print
print rlat

f = 2.*math.pi / 86164.09 * math.sin( math.radians(rlat) )
print 'Coriolis parameter f =',f,' for latitude =',rlat

a = 0.2
print 'neutral mixing height for u*=0.1 m/s would be ', round(a*0.1/(f+1.e-15),1), 'm'

listhmix = []
listh = []
sumhmix = 0.
sumh = 0.
n = 0
nn = 180

infile = open(fn)
```

```
dtstring = ''
dtstringold = ''
newhmix = False
newhabl = False
first = True
outlist = []
for line in infile:
if 'Timing for main:' in line:
fields = line.split()
dtstring = fields[4]
thisdt = dt.datetime.strptime(dtstring, "%Y-%m-%d_%H:%M:%S")
dtstringold = dtstring
newhabl = True
newhmix = True
if first:
startdt = thisdt
else:
time = thisdt - startdt
outlist.append('  '.join([ \
dtstring,  '%.4f'%round(time.total_seconds()/86400.,4) , \
str(round( habl, 1)), str(round( hmix, 1)), str(round( h, 1)), \
'%.2f'%round( ustar, 2)]) )
sumhmix = sumhmix + hmix
sumh = sumh + h
n = n + 1
listhmix.append(hmix)
listh.append(h)
if len(listh) > nn:
listh.pop(0)
listhmix.pop(0)
first = False
elif 'boundary-layer-height' in line and newhabl:
habl = float(line.split()[1])
newhabl= False
elif 'mixing-height' in line and newhmix:
hmix = float(line.split()[1])
newhmix = False
elif 'ustar' in line:
ustar=float(line.split()[1])
h = a*ustar/(f+1.e-15)

fo=open( fnout, 'w')
fo.write('\n'.join(outlist)+'\n')
fo.close()
print 'output written to ',fnout
print 'average values of hmix and h',round(sumhmix/n,1), round(sumh/n,1)
print 'last '+str(nn/30)+'-h mean of hmix and h',round(sum(listhmix)/nn,1), \
```

```
round(sum(listh)/nn,1)
print 'best fit for a=', round(a*sum(listhmix)/sum(listh), 3)
print 'ustar',round(ustar,4)
hx=round(sum(listhmix)/nn,1)
ha=round(sumh/n,1)
ftab=open('htable.txt','a')
ftab.write( ' '.join([str(rlat),str(V),str(hx),str(ha),str(round(ustar,4)), str(round(f,8))]
ftab.close()
```

Bibliography

Andren, A. (1995). The structure of the stably stratified atmospheric boundary layer: a large eddy simulation study. *Quarterly Journal of the Royal Meteorological Society 121*, 961–985.

Arya, S. (1981). Parameterizing the height of the stable atmospheric boundary layer. *Journal of Applied Meteorology 20*, 1192–1202.

Baas, P., F. Bosveld, G. Lenderink, E. van Meijgaarda, and A. Holtslag (2010). How to design single-column model experiments for comparison with observed nocturnal low-level jets. *Quarterly Journal of the Royal Meteorological Society 136*, 671–684.

Banks, R., T. Jordi, J. Baldasano, F. Rocadenbosch, A. Papayannis, S. Solomos, and C. Tzanis (2016). Sensitivity of boundary-layer variables to PBL schemes in thewrfmodel based on surface meteorological observations, lidar, and radiosondes during the HygrA-CD campaign. *Atmospheric Research 176*, 185–201.

Benkley, C. W. and L. L. Schulman (1979). Estimating mixing depths from historical meteorological data. *Journal of Applied Meteorology 18*, 772–780.

Beyrich, F. (1997). Mixing height estimation from sodar data – a critical discussion. *Atmospheric Environment 31*, 3941–3953.

Blackadar, A. (1998). *Turbulence and diffusion in the atmosphere*. Springer.

Boers, R., E. Eloranta, and R. Coulter (1984). Lidar observations of mixed layer dynamics: Tests of parameterized entrainment models of mixed layer growth rate. *Journal of Applied Meteorology and Climatology 23*, 247–266.

Breuer, H., F. Ács, . Horváth, P. Németh, and K. Rajkai (2014). Diurnal course analysis of the WRF-simulated and observation-based planetary boundary layer height. In *Advances in Science and Research*, Volume 11, pp. 83–88.

Burzynski, J., J. Walczewski, and A. Tomaszewska (2004). The calculated mixing height in comparison with the measured data. In *9th Conference on Harmonisation within Atmospheric Dispersion Modelling for Regulatory Purposes*, Volume 2, pp. 24–28.

Chen, S. (2014). Initialization for idealised cases. `http://mmg.atm.ucdavis.edu/atm-225-class-notes/`.

Clifford, S., J. Kaimal, R. Lataitis, and R. Strauch (Eds.) (1994). *Ground-based remote profiling in atmospheric studies: an overview*, Volume 82. IEEE.

Cohen, A. E., S. M. Cavallo, M. C. Coniglio, and H. E. Brooks (2015). A review of planetary boundary layer parameterization schemes and their sensitivity in simulating southeastern U.S. cold season severe weather environments. *Weather and Forecasting 30*(3), 591–612.

Colle, B., M. Sienkiewicz, C. Archer, and D. Veron (2015). Improving the mapping and prediction of offshore wind resources (IMPOWR): Experimental overview and first results. *Bulletin of the American Meteorological Society 97*(8), 1377–1390.

Cuxart, J., A. Holtslag, R. Beare, E. E. Bazile, A. Beljaars, A. Cheng, L. Conangla, M. Ek, F. Freedman, R. Hamdi, A. Kerstein, H. Kitagawa, G. Lenderink, D. Lewellen, and J. Mailhot (2006). Single-column model intercomparison for a stably stratified atmospheric boundary layer. *Boundary-Layer Meteorology 118*(2), 273–303.

Emeis, S., K. Schäfer, and C. Münkel (2008). Surface-based remote sensing of the mixing-layer height – a review. *Meteorologische Zeitschrift 17*, 621–630.

Eresmaa, N., A. Karppinen, S. M. Joffre, J. Räsänen, and H. Talvitie (2006). Mixing height determination by ceilometer. *Atmospheric Chemistry and Physics 6*, 1485–1493.

Fearon, M. G., T. Brown, and G. Curcio (2015). Establishing a national standard method for operational mixing height determination. *Journal of Operational Meteorology 3*(15), 172–189.

Feng, X., B. Wu, , and N. Yan (2015). A method for deriving the boundary layer mixing height from MODIS atmospheric profile data. *Atmosphere 6*, 1346–1361.

Garratt, J. (1994). *The atmosperic boundary layer*. Cambridge University Press.

Garratt, J. and R. Brost (1981). Radiative cooling effects within and above the nocturnal boundary layer. *Journal of Atmospheric Science 38*, 2730–2746.

Garratt, J. R., G. Hess, W. Physick, and P. Bougeault (1996). The atmospheric boundary layer - advances in knowledge and application. *Boundary-Layer Meteorology 78*, 9–37.

Garrett, A. (1981). Comparison of observed mixed layer depth to model estimates using observed temperature and winds, and MOS forecasts. *Journal of Applied Meteorology 20*, 1277–1283.

Ghan, S., L. Leung, and J. McCaa (1999). A comparison of three different modeling strategies for evaluating cloud and radiation parameterizations. *Monthly Weather Review 127*, 1967–1984.

Gómez-Navarro, J., C. Raible, and S. S. Dierer (2015). Sensitivity of the WRF model to PBL parametrisations and nesting techniques: evaluation of wind storms over complex terrain. *Geoscientific Model Development 8*, 3349–3363.

Hariprasad, K. B., C. Srinivasa, A. Bagavath Singha, S. Vijaya Bhaskara, R. Raob, B. Baskarana, and Venkatramana (2014). Numerical simulation and intercomparison of boundary layer structure with different PBL schemes in WRF using experimental observations at a tropical site. *Atmospheric Research 145*, 27–44.

Hashmonay, R., A. Cohen, and U. Dayan (1991). Lidar observations of atmosphere boundary layer in Jerusalem. *Journal of Applied Meteorology 30*, 1228–1236.

Held, I. and M. Suarez (1994, October). A proposal for the intercomparison of the dynamical cores of atmospheric general circulation models. *Bulletin of the American Meteorological Society 75*(10), 1825–1830.

Holton, J. (1979). *An introduction to dynamic meteorology*. Academic Press.

Holtslag, A. and F. Nieuwstadt (1986). Scaling the atmospheric boundary layer. *Boundary-Layer Meteorology 36*, 201–209.

Holtslag, A. A. M. and G.-J. Steeneveld (2011). *Single Column Modeling of Atmospheric Boundary Layers and the Complex Interactions with the Land Surface*, pp. 844–857. New York, NY: Springer New York.

Holzworth, G. C. (1964). Estimates of mean maximum mixing depths in the contiguous united states. *Monthly Weather Review 92*, 235–242.

Hong, S. (2010). A new stable boundary-layer mixing scheme and its impact on the simulated east asian summer monsoon. *Quarterly Journal of the Royal Meteorological Society 136*, 1481–1496.

Hong, S. and J. Dudhia (2006). A new vertical diffusion package with an explicit treatment of entrainment processes. *Monthly Weather Review 134*, 2318–2341.

Hu, X., J. W. Nielsen-Gammon, and F. Zhang (2010). Evaluation of three planetary boundary layer schemes in the WRF model. *Journal of Applied Meteorology and Climatology 49*(9), 1831–1844.

Janjić, Z. (1990). The step-mountain coordinate: Physical package. *Monthly Weather Review 118*, 1429–1443.

Janjić, Z. (2002). Nonsingular implementation of the Mellor-Yamada level 2.5 scheme in the NCEP meso model. *NCEP Office Note 437*.

Janjić, Z. I. (1994). The step–mountain eta coordinate model: Further developments of the convection, viscous sublayer, and turbulence closure schemes. *Monthly Weather Review 122*, 927–945.

Janjić, Z. I. (1996). The surface layer in the NCEP eta model. In *Eleventh Conference on Numerical Weather Prediction*, pp. 333–334. Am. Meteorol. Soc., Norfolk, Va.

Joffre, S. M., M. Kangas, M. Heikinheimo, and S. Kitaigorodskii (2001). Variability of the stable and unstable atmospheric boundary layer height and its scales over a boreal forest. *Boundary Layer Meteorology 99*(3), 429–450.

Jordan, C. (1958). Mean soundings for the West Indies area. *Journal of Meteorology 15*, 91–97.

Kara, A., P. Rochford, and H. Hurlburt (2000). An optimal definition for ocean mixed layer depth. *Journal of Geophysical Research 105*(C7), 16,803–16,821.

Klett, J. D. (1981). Stable analytical inversion solution for processing lidar returns. *Applied Optics 20*, 211–220.

Kunkel, K., E. Eloranta, and S. Shipley (1977). Lidar observations of the convective boundary layer. *Journal of Applied Meteorology*, 1306.

Ladwig, B. (2018). WRF-python documentation release 1.3.0. `https://media.readthedocs.org/pdf/wrf-python/latest/wrf-python.pdf`.

Lilly, D. (1968). Models of cloud-topped mixed-layer under a strong inversion. *Quaterly Journal of the Royal Meteorological Society 94*(292-309).

Mahrt, L., J., C. André, and R. Heald (1982). On the height of the nocturnal boundary layer. *Journal of Applied Meteorology 21*, 90–92.

Markowicz, K. M., P. J. Flatau, A. E. Kardas, J. Remiszewskaj, K. Stelmaszcyk, and L. Woste (2008). Ceilometer retrieval of the boundary layer vertical aerosol extinction structure. *Journal of Atmospheric and Oceanic Technology 25*, 928–944.

Melfi, S., J. Spinhirne, S. Chou, and S. Palm (1985). Lidar observations of vertically organized convection in the planetary boundary layer over the ocean. *Journal of Applied Meteorology and Climatology 24*, 806–821.

Mellor, G. and T. Yamada (1982). Development of a turbulence closure model for geophysical fluid problems. *Reviews of Geophysics 20*, 851–875.

Miller, M. (1967). Forecasting afternoon mixing depth's and transport wind speed. *Monthly Weather Review 95*, 35–44.

Münkel, C. and J. Räsänen (2004). New optical concept for commercial lidar ceilometers scanning the boundary layer. *P. SPIE* (5571), 364.

Nakanishi, M. and H. Niino (2009). Development of an improved turbulence closure model for the atmospheric boundary layer. *Journal of Meteorological Society of Japan 87*, 895–912.

Newsom, R. and R. Banta (2003). Shear-flow instability in the stable nocturnal boundary layer as observed by doppler lidar during the CASES-99. *Journal of Atmospheric Science 60*, 16–33.

Nieuwstadt, F. (1981). The steady state height and resistance laws of the nocturnal boundary layer: theory compared with Cabauw observations. *Boundary-Layer Meteorology 20*, 3–17.

Nieuwstadt, F. (1984). The turbulent structure of the stable, nocturnal boundary layer. *Journal of the Atmospheric Sciences 41*, 2202–2216.

Olesen, H., A. Jensen, and N. Brown (1992). An operational procedure for mixing height estimation. MSTLUFT-A96. National Environmental Research Institute, Denmark.

Ouwersloot, H. and J. Vilà-Guerau de Arellano (2013). Analytical solution for the convectively-mixed atmospheric boundary layer. *Boundary-Layer Meteorology 148*, 557–583.

Pleim, J. (2007). A combined local and nonlocal closure model for the atmospheric boundary layer. *Journal of Applied Meteorology and Climatology 46*, 1383–1409.

Powers, J., J. Klemp, S. W.C., C. Davis, J. Dudhia, D. Gill, J. Coen, and D. Gochis (2017). The weather research and forecasting model: overview, system efforts, and future directions. https://journals.ametsoc.org/doi/10.1175/BAMS-D-15-00308.1.

Rotunno, R. and K. A. Emanuel (1987). An air-sea interaction theory for tropical cyclones. Part II: Evolutionary study using a nonhydrostatic axisymmetric numerical model. *Journal of the Atmospheric Sciences 44*, 542–561.

Samah, A. (1997). Modelling the development of mixing height in near equatorial region. In S. Gryning, F. Beyrich, and E. Batchvarova (Eds.), *The Determination of the Mixing Height - Current Progress and problems. EURASAP Workshop Proceedings.*, Volume R-997, pp. 31–34.

San José, R. and J. Casanova (1988). An empirical method to evaluate the height of the convective boundary layer by using small mast measurements. *Atmospheric Research 22*, 265–273.

Seibert, P., F. Beyrich, S. Gryning, S. Joffre, A. Rasmussen, and P. Tercier (1997). Mixing height determination for dispersion modelling. In B. Fischer, J. Erbrink, S. Finardi, P. Jeanett, S. Joffre, M. Morselli, U. Pechinger, P. Seibert, and D. Thomson (Eds.), *COST ACTION 710 - Final report. Harmonisation of the pre-processing of meteorological data for atmospheric dispersion models.* European Commission.

Seibert, P., F. Beyrich, S. Gryning, S. Joffre, A. Rasmussen, and P. Tereier (2000, July). Review and intercomparison of operational methods for the determination of the mixing height. *Atmospheric Environment 34*, 1001–1027.

Skamarock, B. (2017). Idealized cases: Introduction. `https://www.climatescience.org.au/sites/default/files/WRF_ideal_201711.pdf`.

Skamarock, W., J. Klemp, J. Dudhia, D. Gill, D. Barker, M. Duda, X. Huang, W. Wang, and J. Powers (2008). A description of the advanced research WRF version 3. Technical report, NCAR.

Sorbjan, Z. (1989). *Structure of the atmospheric boundary layer*. Prentice Hall.

Steeneveld, G., B. van de Wiel, and A. Holtslag (2006). Diagnostic equations for the stable boundary layer height: evaluation and dimensional analysis. *Journal of Applied Meteorology and Climatology 46*, 212–225.

Straka, J., R. Wilhelmson, L. Wicker, J. Anderson, and K. Droegemeier (1993, July). Numerical solutions of a non-linear density current: A benchmark solution and comparisons. *International Journal for Numerical Methods in Fluids 17*(1), 1 – 22.

Stull, R. (1988). *An introduction to boundary layer meteorology*, Volume 13. Springer.

Stull, R. (2016). *Practical Meteorology: An Algebra-Based Survey of Atmospheric Science.* University of British Columbia, British Columbia.

Stull, R. B. (1983). A heat-flux history length scale for the nocturnal boundary layer. *Tellus A: Dynamic Meteorology and Oceanography 35*(3), 219–230.

Sugiyama, G. and J. Nasstrom (1999). Methods for determining the height of the atmospheric boundary layer. Technical report, Lawrence Livermore National Laboratory.

Syrakov, E. (2015). General diagnostic equations and regime analysis for the height of the planetary boundary layer. *Quarterly Journal of the Royal Meteorological Society 141*, 2869–2879.

Tang, G., J. Zhang, X. Zhu, T. Song, Z. Liu, J. Zhang, L. Wang, J. Xin, P. Suppan, and Y. Wang (2016). Mixing layer height and its implications for air pollution over Beijing, China. *Atmospheric Chemistry and Physics 16*, 2459–2475.

Tennekes, H. (1970). Free convection in the turbulent Ekman-layer of the atmosphere. *Journal of the Atmospheric Sciences 27*, 1027–1033.

Tennekes, H. (1973). A model for the dynamics of the inversion above a convective boundary layer. *Journal of the Atmospheric Sciences 30*, 558–567.

Tennekes, H. and A. M. Drierdonks (1981). Basic entrainment equations for atmospheric boundary layer. *Boundary-Layer Meteorology 20*, 515–531.

Vickers, D. and L. Mahrt (2004). Evaluating formulations of the stable boundary layer height. *Journal of Applied Meteorology*, 1736–1749.

Vogelezang, D. and A. Holtslag (1996). Evaluation and model impacts of alternative boundary-layer height formulations. *Boundary-Layer Meteorology 81*, 245–269.

Wiegner, M., F. Madonna, I. Binietoglou, R. Forkel, J. Gasteiger, A. Geiß, G. Pappalardo, K. Schaefer, and W. Thomas (2014, 07). What is the benefit of ceilometers for aerosol remote sensing? An answer from EARLINET. *7*, 1979–1997.

Xie, B., J. C. Fung, A. Chan, , and A. Lau (2012). Evaluation of nonlocal and local planetary boundary layer schemes in the WRF model. *Journal of Geophysical Research 117*(12), 1–26.

Xie, B., J. Hunt, D. Carruthers, J. Fung, and J. Barlow (2013). Structure of the planetary boundary layer over Southeast England: modeling and measurements. *Journal of Geophysical Research 118*, 7799–7818.

Zhang, M., R. Somerville, and S. Xie (2016). The SCM concept and creation of ARM forcing datasets. *Meteorological Monographs 57*.

Zilitinkevich, S. (1972). On the determination of the height of the Ekman boundary layer. *Boundary-Layer Meteorology 3*, 141–145.

Zilitinkevich, S., A. Baklanov, J. Rost, A. Smedman, V. Lykosov, and P. Calanca (2002). Diagnostic and prognostic equations for the depth og the stably stratified Ekman boundary layer. *Quarterly Journal of the Royal Meteorological Society 128*, 25–46.

Zilitinkevich, S. and I. Esau (2003). The effect of baroclinicity on the equilibrium depth of the neutral and stable planetary boundary layers. *Quarterly Journal of the Royal Meteorological Society 129*, 3339–3356.

Zilitinkevich, S. and D. Mironov (1996). A multi-limit formulation for the equilibrium height of a stably stratified boundary layer. *Boundary-Layer Meteorology 81*, 325–351.